

Journal Pre-proof

Engineering in-plane mechanics of electrospun polyurethane scaffolds for cardiovascular tissue applications

Samuel K. Luketich, Federica Cosentino, Marzio Di Giuseppe, Giorgio Menallo, Gabriele Nasello, Patrizia Livreri, William R. Wagner, Antonio D'Amore



PII: S1751-6161(22)00050-9

DOI: <https://doi.org/10.1016/j.jmbbm.2022.105126>

Reference: JMBBM 105126

To appear in: *Journal of the Mechanical Behavior of Biomedical Materials*

Received Date: 29 October 2021

Revised Date: 31 January 2022

Accepted Date: 8 February 2022

Please cite this article as: Luketich, S.K., Cosentino, F., Di Giuseppe, M., Menallo, G., Nasello, G., Livreri, P., Wagner, W.R., D'Amore, A., Engineering in-plane mechanics of electrospun polyurethane scaffolds for cardiovascular tissue applications, *Journal of the Mechanical Behavior of Biomedical Materials* (2022), doi: <https://doi.org/10.1016/j.jmbbm.2022.105126>.

This is a PDF file of an article that has undergone enhancements after acceptance, such as the addition of a cover page and metadata, and formatting for readability, but it is not yet the definitive version of record. This version will undergo additional copyediting, typesetting and review before it is published in its final form, but we are providing this version to give early visibility of the article. Please note that, during the production process, errors may be discovered which could affect the content, and all legal disclaimers that apply to the journal pertain.

© 2022 Published by Elsevier Ltd.

Engineering in-plane mechanics of electrospun polyurethane scaffolds for
cardiovascular tissue applications

Samuel K. Luketich¹, Federica Cosentino², Marzio Di Giuseppe², Giorgio Menallo^{1,3}, Gabriele Nasello^{1,4}, Patrizia Livreri⁵, William R. Wagner^{1,4,6,7}, and Antonio D'Amore^{1,2,4,7,8a}

¹McGowan Institute for Regenerative Medicine, University of Pittsburgh, Pittsburgh, PA

²Fondazione RiMED, Italy

³Department of Biomedical Engineering, Worcester Polytechnic Institute, Worcester, MA

⁴Department of Bioengineering, University of Pittsburgh, Pittsburgh, PA

⁵Department of Engineering, University of Palermo, Italy

⁶Department of Chemical & Petroleum Engineering, University of Pittsburgh, Pittsburgh, PA

⁷Department of Surgery, University of Pittsburgh, Pittsburgh, PA

⁸Clinical Translational Science Institute, University of Pittsburgh, Pittsburgh, PA

To be submitted to:

Journal of Mechanical Behavior of Biomedical Materials (IF: 3.239)

^a For correspondence:

Antonio D'Amore, Ph.D.

Group Leader and head of the Tissue Engineering Program –

RiMED Foundation

Via Bandiera, 11

90133 Palermo PA, Italy

Mobile: +393398891218

Email: adamore@fondazionerimed.com

Research Assistant Professor, Departments of Surgery and Bioengineering

McGowan Institute for Regenerative Medicine

University of Pittsburgh

Bridgeside Point Building II

450 Technology Drive, Suite 336.1

Pittsburgh, PA 15219

Tel.: 412-624-5307

E-mail: and78@pitt.edu

Abstract

Effective cardiovascular tissue surrogates require high control of scaffold structural and mechanical features to match native tissue properties, which are dependent on tissue-specific mechanics, function heterogeneity, and morphology. Bridging scaffold processing variables with native tissue properties is recognized as a priority for advancing biomechanical performance of biomedical materials and, when translated to the clinical practice, their efficacy. Accordingly, this study selected electrospinning on a rotating cylindrical target as an apparatus of broad application and mapped the relationship between key processing variables and scaffold mechanics and structure. This information was combined with mechanical anisotropy ranges of interest for the three main categories of tissue surrogated in cardiovascular tissue engineering: heart valve leaflets, ventricle wall, and large diameter blood vessels. Specifically, three processing variables have been considered: the rotational velocity and the rastering velocity of the mandrel and the dry (single nozzle – polymer only) vs wet (double nozzle – polymer plus phosphate buffer saline solution) fabrication configuration. While the dry configuration is generally utilized to obtain micro-fiber based polymeric mats, the wet fabrication is representative of processing conditions utilized to incorporate cells, growth factors, or micro-particles within the fibrous scaffold matrix. Dry and wet processed electrospun mats were fabricated with tangential and rastering velocities within the 0.3-9.0 m/s and 0.16-8 cm/s range respectively. Biaxial mechanics, fiber network, and pore micro-architectures were measured for each combination of velocities and for each fabrication modality (dry and wet). Results allowed identification of the precise combination of rotational and rastering velocities, for both dry and wet conditions, that is able to recapitulate the native cardiovascular tissue anisotropy ratio. By adopting a simple and broadly utilized electrospinning layout, this study

is meant to provide a repeatable and easy to access methodology to improve biomimicry of the in plane-mechanics of heart valve leaflets, ventricular wall, and large diameter blood vessels.

Keywords

electrospinning; electrodeposition; wet processing; cardiovascular tissue surrogates; cardiovascular tissue mechanical properties; cardiovascular tissue morphology.

Journal Pre-proof

1. Introduction

Fibrous materials are ubiquitous in nature. Electrospinning (ES) is one of the most effective micro-fiber deposition techniques able to recapitulate characteristics of fibrous biological materials both from a mechanical and a structural perspective. The popularity of ES is largely a function of a versatile manufacturing process where permanent modifications of the processing apparatus [1], as well as slight alterations of the processing variables during the fabrication process itself, enable the production of scaffolds with a wide array of fiber morphologies. Different topologies result from the combinations of structural variables such as fiber diameter [2], fiber packing density and connectivity [3], fiber orientation and alignment [4, 5], fiber undulation [6], bulk porosity [7], pore size and aspect ratio [8]. These numerous degrees of freedom in the design of the scaffold structure allow for an equally broad array of physical and mechanical properties [9, 10], including anisotropy ratio, strain energy, peak stress, or flexural rigidity. While still suffering from processing artifacts that affect repeatability, ES remains one of the few fiber deposition techniques able to produce an organ/large scale (>1cm) object with high structural organization at the mesoscale (10-100 μm), which is composed of fiber elements with characteristic lengths within the 0.1-10 μm range [11]. By tuning the processing variables, fiber-based scaffolds can be successfully fabricated with a high level of control on the structure-function characteristic and on the fiber network morphology that allows for biomimicry of Extracellular Matrix (ECM) structure. This ability is recognized as a fundamental factor for bioprocessing of engineered tissues as substrate size, scale, stiffness [12], and topography [13] play essential roles in cell adhesion, motility, proliferation, differentiation [14], aging [15], macrophage polarization [16], and host cell recruitment [17].

The kinematics of the mandrel is a processing variable category that directly affects the way polymeric fibers land on the collecting surface and, consequently, their structural arrangement. Specifically, the electrospinning mandrel tangential velocity and rastering velocity have been shown to dictate fiber alignment [4] and fiber intersections [18, 19], respectively. In turn, planar mechanical properties such as tissue anisotropy vary with fiber main angle of orientation and alignment [4]. Similarly, changing the rastering velocity impacts the out of plane, flexural mechanics through the number of fiber intersections [18, 19].

Cardiovascular tissues perform sophisticated tasks in mechanically demanding environments which require complex and hierarchical structural organization. Examples include ventricle region-specific tissue alignment and anisotropy [20] or heart valve and blood vessel functional heterogeneity [21]. For instance, valve leaflet anisotropy is generated from collagen alignment within the fibrosa layer [22, 23], ventricle anisotropy is mainly produced by aligned cardiomyocytes [24, 25], while vascular anisotropy is originated by highly aligned collagen fibers within the tunica media [26, 27]. Mechanical anisotropy in these examples, as well as in many other soft tissues, is one of the most crucial factors for structural integrity and organ function [26]. As such, it was selected in this study as the preferred, targeted variable for the biomimicry of cardiovascular tissue. Two main variables were considered to fine tune mechanical anisotropy: the tangential and the rastering velocity. Since different scaffold types may require the combination of polymer fiber stream with a secondary stream during the fabrication, the concurrent electro-spraying of a wet component such as: cell media, cell solution, buffer solution, or micro-particle solution was considered as a third variable for the processing. In particular, wet processing has been demonstrated to overcome the limited cell infiltration that represents a common drawback for electrospun engineered scaffolds [28, 29].

The objective of this study was to map the relationship between key processing variables and scaffold mechanics and structure and enable biomimicry of cardiovascular tissue planar mechanics. Three processing variables have been considered: the rotational velocity and the rastering velocity of the mandrel and the dry (single nozzle – polymer only) versus wet (double nozzle – polymer plus phosphate buffer saline solution) fabrication configuration.

The structure and function characteristics of each scaffold resulting from the combination of these processing variables were assessed using scanning electron microscopy, digital image analysis, and biaxial mechanical testing. The results allow the identification of the precise combination of rotational and rastering velocities for both dry and wet conditions that is able to recapitulate native tissue anisotropy for the three main clinically relevant applications in cardiovascular tissue engineering: heart valve leaflets, ventricular wall, and large blood vessels. This study provides a repeatable and easy to access methodology to identify tangential and rastering velocities values for both wet and dry electrospun scaffold processing able to recapitulate the planar mechanical response of cardiovascular tissues. While the results focused on heart valve leaflets, ventricular wall, and large blood vessels, the presented methodology can be broadly extended to other soft native tissues.

2. Materials and Methods

2.1 Synthesis of poly (ester urethane) urea

Poly(ester urethane)urea (PEUU) was synthesized using a two-step polymerization from polycaprolactone diol (PCL, $M_n = 2000$, Sigma-Aldrich), 1,4-diisocyanatobutane (BDI, Sigma-Aldrich), and 1,4-diaminobutane (putrescine, Sigma-Aldrich), details were described in [30]. The molar ratio of PCL: BDI: putrescine was set as 1:2:1. In brief, following toluene distillation, the

PCL diol was dissolved in dimethyl sulfoxide (DMSO, Sigma-Aldrich) and reacted with BDI in the presence of the stannous octoate ($\text{Sn}(\text{Oct})_2$, Sigma-Aldrich) catalyst to form the prepolymer. In the second step, putrescine was added as the chain extender and left to react overnight. Deionized water was used for precipitation of the PEUU and was followed by the drying of the precipitated PEUU in a vacuum oven for the next 3 days.

2.2 Electrospun scaffold fabrication

PEUU scaffolds were fabricated through a one- or a two-stream electrospinning process as described in [28] and illustrated by the schematic provided in **Figure 1A**. The electrospinning collecting surface was a rotating cylindrical mandrel of 114 mm in diameter. The deposition area was concentrated at the center of the mandrel by setting a longitudinal rastering span of 3 cm. PEUU was dissolved in 1,1,1,3,3,3-hexafluoro-2-propanol (HFIP, Oakwood Chemicals) at 12% w/v. The single-stream fabrication modality (dry) only involved the electrospinning of the polymer solution and utilized the following processing parameters: a polymer voltage of 12 kV, a polymer flow rate of 1.5 ml/hr, a polymer–injector gap distance of 13.5 cm, and a mandrel voltage of -4 kV. The two-stream electrospinning fabrication (wet) utilized identical polymer electrospinning conditions, but it also involved a secondary stream component of phosphate-buffered saline (PBS) solution which was electro-sprayed with a voltage of 14 kV, a PBS flow rate (secondary stream) of 1.2 ml/hr, and a PBS gap distance of 5 cm. As the collecting target could only rotate around its major axis and translate longitudinally, its kinematics was controlled only by two processing variables: the mandrel tangential velocity and the mandrel rastering velocity.

These two parameters independently dictate structural anisotropy [31, 32] and fiber intersection density [18, 19]. In order to map the full range of values of physiological relevance for isotropic and anisotropic cardiovascular (anisotropy ratio larger than 1) tissue, tangential velocities were set equal to 0.3, 1.5, 3.0, 4.5, 9.0 m/s. A fabrication conducted with a tangential velocity of 1.5 m/s would produce an isotropic, random arrangement of fibers with AR equal to 1 whereas a tangential velocity of 4.5 m/s would induce an oriented fiber arrangement with $AR > 1$ [4]. Similarly, rastering velocities were set equal to 0.16, 2.5, 8.0 cm/s, this corresponds to a range of [0.071 – 0.12] number of fiber intersections/mm² that was previously measured for engineered or native cardiovascular tissue such as in [19] [8].

These fifteen combinations of tangential and rastering velocities were studied under dry (polymer electrospinning only) and wet (polymer electrospinning and PBS electro-spraying) fabrication conditions that represented the third variable (**Figure 1**) investigated in the study. [4, 18, 19]. The processing variables space (V_T , V_R , *Wet/Dry*) investigated in this study is illustrated in **Figure 1B**. While dry/wet condition, as well as tangential and rastering velocities, were different for each of the points within the processing space the remaining processing variables: gap distances, flow rates, and voltages remained unmodified, each sample fabrication required a polymer deposition time of 1.5 hrs.

2.3 Characterization of in-plane mechanics via biaxial mechanical testing

Sample thickness was measured with a dial indicator gage (Starrett, Athol, MA) and averaged among 5 different locations (Table 1).

In-plane tensile mechanical properties of the processed polymeric scaffolds and cardiovascular native tissues (**Figure 1B**) were evaluated using equi-stress biaxial testing as described in [4, 19,

33]. Briefly, 10 mm × 10 mm samples were obtained from each specimen. Next, four marker dots ~1 mm in diameter positioned at the corners of a ~2 mm × 2 mm square in the sample center were utilized to calculate the deformation gradient tensor. Samples mounted on the device were anchored by sutures on edge using four equidistantly placed small surgical fishhooks. To maintain the stress and strain states uniform in the central region, the hooks were located away from the outer edges to avoid the effects of specimen grips [4, 19]. These sutures were attached to the four electromagnetic motors of the biaxial system, aligning circumferential and longitudinal edges with the direction of stretching. Samples were loaded into a custom-made biaxial testing device and tested in PBS at ~23°C for 10 cycles with an unloading and loading time of 15 seconds/cycle. Every sample ($n \geq 3$ /group) was preconditioned and then tested in Lagrangian equi-stress control to peak stress of 418.9 kPa. This value was identified [34] as appropriate to elicit physiologically relevant strain levels (1.2 for left ventricle wall [35, 36], 1.6 for heart valve leaflets [37], 1.5 for large blood vessels [38, 39]). During the biaxial test, a constant ratio of loads was maintained between the two directions (circumferential and longitudinal). Post-processing was completed using a custom MATLAB (MathWorks, Natick, MA) script with the reference point being the free-float marker positions after preconditioning. The 2nd Piola- Kirchhoff stress \mathbf{S} [kPa] was reported.

Strain energy was also calculated utilizing a custom-made code developed in MATLAB in which the algorithm applies a fifth-order polynomial fitting to each experimental biaxial stress-stretch curve and then integrates the area under the curve from 0 kPa to 440 kPa [19].

The stress-strain product defines the work per volume. This energy density is related to the deformed volume, and it is expressed as [19]:

$$\psi = \int_1^{\lambda_1} S_{11} d\lambda_1 + \int_1^{\lambda_2} S_{22} d\lambda_2$$

Where, \mathbf{S} is the Lagrangian stress and λ is the stretch defined by the ratio of the l current length, l , to the initial unstressed length, L , $\lambda = \frac{l}{L}$. Subscripts 1 and 2 refer to the circumferential and longitudinal direction, respectively.

2.4 Characterization of in-plane mechanics via analysis of mechanical anisotropy

The anisotropy ratio which is a common metric for anisotropy was selected to study the impact of the different processing variables on the in-plane behavior of the electrospun mats. Anisotropy was studied by calculating the anisotropy ratios (ARs) of the scaffolds under biaxial loading and by comparing the measured values with anisotropy ratios of native cardiac tissue. AR was defined as the ratio of the Lagrangian's stretches during equi-stress biaxial testing [40-42] using Eq. 1:

$$AR = \frac{\lambda_{LD}}{\lambda_{CD}} \quad (\text{Eq. 1})$$

where λ_{LD} and λ_{CD} are the stretches in the longitudinal and circumferential directions, respectively. AR in healthy cardiac tissue varies considerably based on the tissue type, anatomical location, and based on the different stress levels being applied. Accordingly, in order to properly engineer in-plane mechanics and match native tissue mechanical anisotropy, the AR was calculated for each of the scaffold group at different stress levels. More specifically, every scaffold was tested above 400 kPa to fully cover the 1-1.4 Lagrangian's stretch level. Next, AR was calculated at four stress levels (11.0 kPa, 44.1 kPa, 220.5 kPa, 418.9 kPa) for each fabrication condition, these values allowed to cover deformations observed in the healthy porcine left ventricle wall (0 - 0.25 [43]), heart valve leaflets (0.1 - 0.40 [20]), or large blood vessels such as the descending aorta or the carotid arteries (-0.1 - 0.2 [44, 45]). A detailed description of the method utilized to calculate scaffold AR at a desired stress level that would correspond to the AR measured for healthy cardiac tissue, within physiological strain conditions, is provided in **Supplemental Figure 1**. During the

first step of the process, scaffold specimens are tested under equi-stress biaxial conditions. In step 2, the AR is calculated at the prescribed stress levels based on experimental data and on Eq. 1. In step 3, the experimentally derived ARs and their related stress values are linearly interpolated. Finally, in step 4, the AR vs. stress characteristic is utilized to estimate AR at a specific stress value that would match the maximum stress utilized to elicit physiologically relevant strain in native cardiac tissue. For instance, the example provided in **Supplemental Figure 1** extracts scaffold AR of 1.19 corresponding to a peak stress of 54kPa that was utilized to produce a stretch range of 1-1.3 in a descending aorta (**Figure 5**). The list of native tissue ARs measured in this study and utilized for the engineering of electrospun mats with matching biaxial mechanics are provided in **Table 2** and include porcine left ventricle [46], porcine arteries [47], and porcine heart valve leaflets [8].

While the mandrel tangential velocity is the electrospinning variable directly affecting scaffold fiber orientation [4] and as a consequence affecting scaffold mechanical anisotropy, the rastering velocity has a direct impact on fiber intersection density [18, 19]. In turn, this microstructural feature dictates scaffold bending rigidity. The current study also aimed to understand the interplay between mandrel tangential and rastering velocity. Towards this end, a linear regression model [8] with interactions variables as described in Equation 2, was implemented in Python (Python Software Foundation, Wilmington, DE). The model interpolated ARs, tangential, and rastering velocities for both the dry and the wet electrospinning configurations.

$$AR = c_0 + a_1 \cdot x_1^2 + a_2 \cdot x_1 \cdot x_2 \quad (\text{Eq. 2})$$

Last, to identify the appropriate combination of processing variables that are able to duplicate native cardiovascular tissue anisotropy (**Figure 5**), the interpolated $AR-V_T-V_R$ surfaces were intersected with the ARs of the cardiovascular tissue of interest (**Figure 6**).

2.5 Characterization of micro-structure via scanning electron microscopy and digital image analysis

Scanning electron microscopy (SEM) and digital image analysis [2] were utilized to fully characterize the microstructure of the polyurethane scaffolds. Scaffold samples of 3 mm × 6 mm were sputter-coated with 4.5 nm of Pd/Au. Images (n=5/sample/group) were captured with a JSM 6335F SEM (JEOL, Peabody, MA) at an 850× magnification. Fiber network architecture, more specifically fiber intersection density and pore size, were quantified using the automatic image analysis algorithm validated and developed by our group. This image analysis technique is mainly based on morphological procedures, and it allows for the full characterization of the fiber network and pore meso and microstructure.

Similarly, the main angle of fiber orientation and the correspondent level of fiber alignment were quantified using a different algorithm that was described in [48] and strictly focuses on detecting the dominant alignment of a structure regardless of its fibrous or amorphous topology. This method was derived from Chaudhuri et al [48] and utilizes the intensity gradient to capture the edges of the object of interest at the characteristic scale length which, in this study, was the microscopic scaffold fiber. The OI defined as the average over all fiber segments of $\cos^2 \theta$ (COS OI), where θ represents the angle between a fiber segment and the direction of supposed alignment [49, 50], was utilized as the metric for fiber alignment. [2, 49, 50]. An OI of 0.5 is associated with a random fiber alignment, whereas an OI of 1.0 indicates perfectly parallel and aligned fibers [51].

2.6 Statistical Analysis

The results of this study are presented as mean \pm standard error of the mean. Statistical analysis was performed using SigmaPlot (Systat Software, San Jose, CA). A t-test was used to identify statistically relevant differences of anisotropy in the biaxial mechanical tests. Two-way analysis of variance (ANOVA) followed by Bonferroni correction was used for all of the other analyses, with the two factors being the tangential and the rastering velocity. Differences at $p < 0.05$ were considered to be statistically significant.

3. Results

3.1 Characterization of in-plane mechanics via biaxial mechanical testing

The biaxial mechanical response of the polyurethane scaffolds is shown in **Figures 2-3**. Scaffolds were fabricated by setting 30 different electrospinning configurations, obtained with the permutation of the three variables, V_R , V_T , and *Wet/Dry*. As the tangential velocity was raised, the mechanical compliance over the longitudinal direction of the scaffold increased for both dry and wet fabrications. Every dry fabrication configuration conducted at $V_T \geq 3.0$ m/s produced significantly different stretch values at peak stress. Similarly, every wet fabrication configuration conducted at $V_T \geq 4.5$ m/s produced significantly different stretch values at peak stress. Overall, the compliance of the scaffolds along the longitudinal direction was smaller for the wet processing when compared to the dry, this was consistent with the reduced control on scaffold morphology generally observed when a secondary stream is interfering with the main polymer stream during the electrodeposition.

A comparison of the strain energy of the different polyurethane scaffold groups is presented in **Figure 4**. Overall, increasing tangential velocity produced a decrease in strain energy over the circumferential direction, an increase in strain energy over the longitudinal direction, and an

increase in the total strain energy for both dry and wet fabrication. This is a direct consequence of the increased anisotropy dictated by the stronger alignment of the fibers. In contrast, and consistently with the analysis of the biaxial response, the rastering velocity did not affect the strain energy. In Table 3 is reported the average circumferential, longitudinal and total strain energy of the native cardiovascular tissues considered in this study: heart valve leaflets, ventricular wall, and large blood vessels (carotid artery and descending aorta).

3.2 Characterization of in-plane mechanics via analysis of mechanical anisotropy

The AR was calculated for all of the dry and wet electrospinning configurations at 11.0 kPa, 44.1 kPa, 220.5 kPa, and 418.9 kPa, following a process illustrated with additional detail in **Supplemental Figure 1**. The value of ARs calculated at peak stress for native porcine cardiac tissue, the linear equations, and their R^2 are reported in **Table 4**. These equations were utilized to calculate ARs values that represent the ranges of interest that are requested for a scaffold to duplicate the anisotropy of native porcine left ventricle wall, heart valve leaflets, and large blood vessels. These values are presented in **Figure 5 A-C** as color bands and were based on peak stress of 5.3 kPa, 44.1 kPa, and 54 kPa, respectively.

Combined effects of tangential and rastering velocities on AR were also presented in the $AR-V_T-V_R$ space as 3D surface plot (**Figure 6**). A linear regression model was utilized to fit the experimental data obtained characterizing the scaffold mechanics and reported an $R^2 > 0.95$ (**Table 5**). Surfaces in **Figure 6** represent the range of scaffold anisotropy that can be achieved by combining different values of rastering and tangential velocities. The red planes, that are perpendicular to the AR axis, represent the anisotropy of the three key examples of cardiovascular tissue considered in this work: porcine left ventricular wall, heart valve leaflets tissue and large

blood vessels. The red lines highlight the intersection of the desired native tissue AR with the processed scaffold surfaces, therefore they identify the specific combination of processing variables (V_T , V_R , Dry/Wet) requested to mimic native tissue anisotropy.

3.3 Characterization of micro-structure via scanning electron microscopy and digital image analysis.

Representative scanning electron micrographs of the scaffolds obtained from the 30 different electrospinning configurations are provided in **Figures 7-8**. A small inset in the micrograph upper left corner ($V_R=0.16$ cm/s, $V_T=0.3$ and 9.0 m/s; $V_R=8$ cm/s, $V_T=0.3$ and 9.0 m/s) shows the corresponding biaxial mechanical response of the scaffold that was fully reported in **Figure 3**. This was included to better highlight the structure-function coupling between the fiber alignment and the mechanical anisotropy. An increased tangential velocity corresponded to an increased alignment of the fibers in the scaffold for both dry and wet fabrications.

In addition to the qualitative comparison of the different fabrication configurations, quantitative analysis of the micrographs was performed using a custom MATLAB algorithm[2]. Results are shown in **Figures 9-10**. For both figures, panels A-B show representative fiber network and pores as identified by the algorithm and used to calculate, fiber intersection density and pore size. Panel C provides an example of the results produced by the second algorithm that was utilized [2] to detect fiber alignment and angle of fiber orientation. Overall, **Figure 9D** shows a decrease in normalized fiber intersection density with an increase in tangential velocity. In addition, for dry fabrication, there was a general decrease in fiber intersection with increased rastering velocities.

4. Discussion

ES, melt electrowriting [52], jet-spinning [53], and double component deposition [8] are among the few processing techniques that have the ability to recapitulate the characteristics of native fibrillar tissue and micro fiber based synthetic materials from both a mechanical and a structural perspective (**Figure 11**) [19, 54]. Key structural-mechanical properties of micro fiber based scaffolds include: I) micro fiber alignment and orientation, which dominates in-plane scaffold deformation and anisotropy [21]; II) fiber diameter, which dictates the pore size and therefore influences host cell infiltration [55, 56]; III) engineered construct shape and size, which are macro-scale parameters that determine functional efficiency of a prosthesis [57]; IV) tensile modulus, which is a key factor for tissue motility, for the mechanobiology of the cells that infiltrated the scaffold, their related collagen synthesis and elaboration [56, 57]; and V) fiber intersection density and connectivity, which are related with bending rigidity [18] and scaffold mechanical behavior at the mesoscopic scale [13]. As ventricular walls, heart valve leaflets, and large blood vessels function mainly as a membrane [33, 58], in-plane mechanics are generally considered a predominant element in the design and processing of engineered cardiovascular tissue. Accordingly, this work addresses in detail mechanical anisotropy and how this parameter can be fine-tuned in a highly reproducible ES layout to duplicate native cardiovascular tissue behavior.

4.1 Characterization of in-plane mechanics via biaxial mechanical testing

While tensile modulus is an intrinsic property that can be tailored at the molecular level, anisotropy can be controlled at the supra-molecular level by the topology of the fiber network and, as such, it can be dictated by the processing variables. Cardiovascular tissue engineering applications require high control of scaffold structural and mechanical features to match native cardiovascular tissue properties [52, 59-62], which are dependent on the tissue-specific function

and guaranty its mechanical homeostasis. This study mapped (**Figure 1**) the relationship between three key processing variables: I) tangential velocity, II) rastering velocity, III) and dry vs wet processing and scaffold anisotropy. Although previous studies observed that tangential and rastering velocity are independent variables[8], both velocities were considered to explore the relationship between mandrel kinematics and scaffold anisotropy.

Similar to previous work [4, 63], an increase in the tangential velocity of the mandrel produced a larger fraction of circumferentially aligned fibers, increased the compliance of the scaffold along the longitudinal direction and consequently increased the strain energy. More specifically, by increasing the velocity from 1.5 m/s to 3.0 m/s in the dry fabrications, a significant difference in compliance was observed between the two axes (**Figure 2**). This was consistent with the results from Courtney et al. [4], who identified 2.0 m/s as the threshold velocity value for the anisotropy to become a linear function of the tangential velocity. While with a slightly higher threshold, due to the variability introduced by the secondary stream, similar effects were observed for the wet fabrication (**Figure 3**).

The strain energy of the scaffold was calculated according to [22] as the area underneath the biaxial stress-stretch curve (**Figure 4**). Values reported for the $V_T=0.3$ m/s groups, both dry and wet, were all below 30 kJ, this was consistent with previous studies [19].

As discussed in [8, 18, 19] the rastering velocity had no significant effects on the anisotropy for both dry and wet fabrication (**Figure 2 and Figure 3**), this decoupled the role of the two kinematic variables and confirmed the capacity of this polymer fiber deposition process to independently control anisotropy via the tangential velocity and the bending rigidity by changing the rastering velocity [8, 18].

A quantitative comparison between electrospun mats and native cardiovascular tissues' strain energy was performed. Results showed that the range of average circumferential, longitudinal and total strain energy values stored by native cardiovascular tissues under equibiaxial loading (0.07 - 0.3 kJ for left ventricle, 4.92 - 30.65 kJ for heart valves, 14.34 - 29.39 kJ for carotid artery, and 13.53 - 17.18 kJ for descending aorta) can be reproduced by fine tuning the processing variables of both dry and wet electrodeposition process, as shown in Figure 4. Surprisingly, left ventricle stored a low amount of strain energy in both directions compared with the other native cardiovascular tissues, although this measure might be affected by the low number of samples.

A 3D space ($AR-V_T-V_R$) was developed as shown in **Figure 6** to investigate the influence of both velocities. While there are numerous native tissues with anisotropic planar mechanics [26, 27] that could potentially be duplicated using these curves, this study was specifically designed to aid in the development of cardiovascular tissue surrogates. A comparison between scaffold properties and mechanical properties from porcine left ventricle wall [30], heart valve leaflets [63], and large blood vessels [28] is provided in (**Figure 5D-F** and **Figure 6**). Specifically, the methodology presented provided rastering and tangential velocity values required to fabricate wet or dry scaffolds matching cardiovascular tissue ARs.

4.2 Microstructure

The structure of the electrospun scaffolds was evaluated through scanning electron microscopy and digital image analysis as in [33, 34]. Representative SEM images in **Figures 7-8** showed increased fiber alignment associated with increased tangential velocity. This is consistent with the biaxial response and the anisotropy ratios reported in **Figures 7-8**. The inset image of the biaxial response illustrates further the effect of fiber alignment on the biaxial mechanical response.

Four structural features were selected and studied based on their influence on planar mechanical properties and cellular infiltration: fiber intersection density (**Figures 9A** and **10A**), pore size (**Figures 9B** and **10B**), main fiber orientation, and fiber alignment (**Figures 9C** and **10C**). For the dry fabrications, an overall decrease in fiber intersection density with increased tangential velocity (**Figure 9D**) was reported. This effect can be considered a function of a more aligned fiber network [19]. Consistently with previous studies [8, 18, 19] for the dry fabrications, fiber intersections decreased with increased rastering velocity (**Figure 9D**). No significant correlation was found between pore size and tangential or rastering velocity for dry fabrications (**Figure 9E**). For wet fabrications (**Figure 10E**), pore sizes were significantly increased only at the highest translational and rastering velocities. As expected [4], a significant increase in the level of fiber alignment with increasing tangential velocity was observed for both dry and wet conditions (**Figure 9G** and **10G**).

4.3 Dry and wet fabrications

To address the limited cellular infiltration which is widely considered a limiting factor in electrospun scaffolds, wet processing was utilized in this study as a simple alteration of the fabrication apparatus that leads to an electrospun scaffold with a fiber network more prone to be populated by host cells. A comparison between acellular dry and wet processing, that emphasizes this effect, is presented in [28]. More importantly, wet processing conditions are equivalent in terms of flow rate, gap, voltage gap, and mandrel kinematics to those utilized for cell or micro-particle integration via electro-spray [39]. As such this study can be utilized to serve the broader audience interested in controlling anisotropy in a cell seeded construct. Previous studies have utilized a secondary stream electro-spraying PBS [40], a secondary polymer stream [41], extracellular matrix gel integration [64], or concurrent electro-spraying of a cell solution [46].

Hashizume et al. [28] demonstrated substantially higher cellular infiltration and scaffold remodeling in wet constructs for abdominal wall replacement compared to dry electrospun scaffold. The overall morphology of the two acellular scaffold types was equivalent. This qualitative observation was reinforced by the quantitative information presented in this study (Figures 9-10). We previously speculated that the higher infiltration capacity in wet processed scaffolds could be attributed to the wet environment that reduces the local concentration of solvent and therefore reduces the probability that two overlapping fibers can form a mechanical bond during the formation of the polymer fiber network. The mechanism of wet deposition maintains the fibrillar network structure in shape and size as measured in dry processed scaffolds but reduces the actual fiber connectivity facilitating cell infiltration [28, 65]. This observation is supported by the more tortuous fiber arrangement observed in wet processing and by the reduced stress concentration observed for wet processed scaffolds. However, the major advantage in terms of cellularity, for both cell seeded constructs or acellular wet processed scaffolds comes with the significant cost of a reduced level of control on structure and function. Accordingly, this study also aimed to characterize to what extent wet processing affects the capacity to control anisotropy and microstructure. Consistent with previous work [4, 8] increasing mandrel velocity in dry fabrication produced linear increments of anisotropy ratio for values above 2 m/s. In contrast, an increase in mandrel tangential velocity for wet processing resulted in a reduced capacity to induce fiber alignment (**Figures 7, 8**) with significant anisotropy (**Figures 2, 3**) and increased strain energy (**Figure 4**) only for velocities higher than 4.5 m/s.

4.4 Limitations

While previous structure-function studies de-coupled the effects of tangential and rastering velocities by associating tangential velocity with planar mechanics [4, 63] and rastering velocity with flexural mechanics [18, 19, 63], this work did not further investigate bending rigidity and focused exclusively on the planar mechanical properties of polymeric, fiber based scaffolds. Additional tangential velocity values within the 4.5 m/s - 9.0 m/s range could have been considered in order to increase the precision of the 3D plane interpolation for the wet processing (**Table 4**) where few R^2 resulted smaller than 0.9.

The ARs reported herein are based on a rather simple geometry of a cylindrical mandrel. Recapitulating mechanical anisotropy on a non-planar scaffold with anatomy inspired [66, 67] or more complex geometries [67] would likely require re-characterizing the fabrication parameters. Yet, cylindrical mandrels of a different diameter would not require further characterization, as different rotational speeds allow one to reach identical tangential velocity ranges. Control over anisotropy by manipulating other electrospinning parameters that are not related to the kinematics of the mandrel [68-70] remains a more complex and yet valuable option that was not considered in this study. Another limitation is that mechanical properties at cell length scale were not investigated. Mechanical properties of the scaffolds play an important role in cardiovascular tissue applications. It is known that microscopic mechanical properties guide cell response. Cells interact with the extracellular matrix (ECM) at the micro and mesoscale, therefore, scaffold's structure and mechanics at these scales should be considered for the biomimicry of native cardiovascular tissue. Investigating scaffold's mechanical behavior at different length scales will provide more precise and accurate control of mechanobiology in cardiovascular tissue engineering.

5. Conclusions

In this study, the inter-relationship between key ES processing variables and fibrillar scaffold structure-function was characterized. In order to provide a reproducible and easy to access methodology to improve biomimicry of cardiovascular tissue planar mechanics, a simplified fabrication layout is discussed. A cylindrical shape mandrel was selected as a commonly adopted collecting target for fiber deposition. Mandrel kinematics prescribed by rastering and tangential velocities were selected as highly controllable key parameters, and a third processing variable: wet versus dry deposition was also discussed. The latter parameter allows extension of the methodology to both acellular and cell seeded or microparticle integrated engineered constructs. Given the planar nature of the biomechanical behavior of native and engineered cardiovascular tissue, anisotropy was considered as one of the most relevant mechanical properties. Accordingly, the relationship between anisotropy ratio - rastering velocity - tangential velocity and - wet vs. dry deposition is provided via multi-dimensional processing maps able to identify specific values to recapitulate planar mechanics of heart valve leaflets, ventricular wall, and blood vessels.

Acknowledgments

This work was financially supported by the RiMED Foundation and by 4FRAILTY project “Sensoristica intelligente, infrastrutture e modelli gestionali per la sicurezza di soggetti fragili” – ARS01_00435 – CUP B6618000250005 granted by the Italian Ministry of Research under the National Research Programme PON Ricerca e Innovazione 2014-2020 e FSC – Action II – Objective 1b. This project has received funding from the European Research Council (ERC) under the European Union’s Horizon 2020 research and innovation program (grant agreement No 101002561 “BIOMITRAL”). The authors would like to thank Dr S. Watkins and the Center for

Biologic Imaging at the University of Pittsburgh for providing guidance and access to its advanced imaging facility.

Figure Captions

Figure 1. Schematic of the processing layout and design space. **A)** Electrospinning layout for single (dry) or two-stream (wet) fiber deposition modality. The secondary stream for the wet component, which in this study was PBS, is removed for single-stream (dry) fabrications where only the polymer source is active during the deposition process. For the wet processing, a concurrent deposition of polymeric fibers and electro-spraying of a liquid solution is obtained by activating the two streams simultaneously. This may include the integration of a cell as well as a micro-particle solution. **B)** Schematic of the three processing variables considered in this study: mandrel tangential velocity (0.3 m/s, 1.5 m/s, 3.0 m/s, 4.5 m/s, 9.0 m/s), mandrel rastering velocity (0.16 cm/s, 2.5 cm/s, 8.0 cm/s), and dry vs. wet processing modality. Each intersection of the three variables within the design space represents a processing modality that was investigated in the study.

Figure 2. Biaxial mechanics of fibrillar scaffolds processed with the dry deposition modality. Biaxial mechanical response of dry processed scaffolds obtained with the fifteen combinations of tangential and rastering velocities investigated in the study. These values were selected to fully cover physiologically relevant levels of anisotropy for cardiovascular tissue. Both velocities were considered to explore the relationship between mandrel kinematics and scaffold anisotropy. Statistically higher compliance of the scaffold is reported at higher tangential velocity.

Figure 3. Biaxial mechanics of fibrillar scaffolds processed with the wet deposition modality.

Biaxial mechanical response of wet processed scaffolds obtained with the fifteen combinations of tangential and rastering velocities investigated in the study. Statistically higher compliance of the scaffold is only reported for tangential velocity equal to or higher than 4.5 m/s. This was consistent with the reduced level of control in fiber deposition produced by the presence of a secondary wet stream.

Figure 4. Strain energy analysis for scaffolds processed with the dry and wet modalities.

Total strain energy for the A) dry and B) wet fabrication configurations were calculated as the area underneath the biaxial stress-stretch curve of scaffolds processed with tangential and rastering velocities within the 0.3-9.0 m/s and 0.16-8 cm/s range, respectively. An increase in the tangential velocity produced an increase in strain energy over the longitudinal direction, this resulted in an overall increase in the total strain energy for both dry and wet fabrications. This result was in agreement with the analysis of the biaxial response, where the rastering velocity did not affect the strain energy nor the stiffness over the circumferential direction.

Figure 5. Quantitative comparison of mechanical anisotropy for the fibrillar scaffolds and native cardiovascular tissues.

Anisotropy ratio (AR) of dry and wet electrospun fibrillar scaffolds overlaid with **A)** porcine ventricle wall AR, **B)** porcine heart valve leaflets AR, and **C)** porcine large blood vessels AR. AR for the three tissue types were calculated at 5.3 kPa, 44.1 kPa, and 54.0 kPa, respectively. The different ranges of anisotropy are presented as color bands. The biaxial mechanical response utilized to calculate ARs are presented in **D)** for porcine ventricle wall, in **E)**

for porcine heart valve leaflets [adapted from (D'Amore, Luketich et al. 2018)], and in **F**) for porcine large blood vessels .

Figure 6. 3D surface plot of the AR- V_T - V_R processing space.

A 3D processing space (AR - V_T - V_R) correlating the kinematics of the mandrel with the anisotropy ratio was utilized to investigate the effects of mandrel tangential and rastering velocity on wet and dry electrospun scaffold in terms of in-plane mechanical response. The ARs of the fifteen electrospinning configurations (blue circles) represent the discrete experimental points that were interpolated using a regression function (blue surfaces) to create continuous AR surfaces. The red lines highlight the intersection between targeted native tissue ARs (red iso-anisotropy ratio surfaces) with the processed scaffold surfaces. This process and the resulting intersection lines identify the specific combination of processing variables (V_T , V_R , *Dry/Wet*) requested to mimic native tissue anisotropy. 3D processing spaces for the biomimicry of ventricle wall, heart valve leaflets, and large blood vessels are reported in **A**), **B**), and **C**) respectively.

Figure 7. Qualitative analysis of dry processed scaffold topology via scanning electron microscopy. Representative SEM images of fibrillar scaffolds from dry electrospun processing showed different levels of fiber alignment for each of the processing parameter combinations. Overall, the fiber alignment increased with increasing tangential velocity while it remained insensitive to changes in the rastering velocity. Inset: Biaxial mechanical response from the corresponding fabrication conditions, as shown in Figure 2, highlights how mechanical anisotropy is coupled with fiber alignment.

Figure 8. Qualitative analysis of wet processed scaffold topology via scanning electron microscopy. Representative SEM images of fibrillar scaffolds from wet electrospun processing at 850× showed different levels of fiber alignment for each of the processing parameter combinations. Overall, the fiber alignment increased with increasing tangential velocity while it remained insensitive to changes in the rastering velocity. Yet, the control on fiber structure was limited if compared with the dry processing as the fiber alignment was associated with increasing tangential velocity only for tangential velocity equal to or higher than 4.5 m/s.

Figure 9. Quantitative analysis of dry processed scaffold topology via digital image processing. The fiber network analysis algorithms presented in [2, 48] was used to identify **A)** scaffold fiber network, **B)** pore structure, and **C)** fiber orientation. A quantitative comparison is provided for **D)** fiber intersection density, **E)** pore size, **F)** main angle of alignment and **G)** orientation index. The fifteen different combinations of variables utilized as experimental points to construct the processing space in Figure 6 were analyzed. Only the statistical differences among the different topologies of the scaffold groups are highlighted, intra-group differences are not presented for improved clarity of the visualization. Yet, no significant nor consistent trend can be attributed to intra-group differences in terms of rastering velocity.

Figure 10. Quantitative analysis of wet processed scaffold topology via digital image processing. The fiber network analysis algorithms presented in [2, 48] was used to identify **A)** scaffold fiber network, **B)** pore structure, and **C)** fiber orientation. A quantitative comparison is provided for **D)** fiber intersection density, **E)** pore size, **F)** main angle of alignment and **G)** orientation index. The fifteen different combinations of variables utilized as experimental points

to construct the processing space for the wet fabrications in Figure 6 were analyzed. Similar to the dry processing only the statistical differences among the different topologies of the scaffold groups are highlighted, intra-group differences are not presented for improved clarity of the visualization. Yet, no significant nor consistent trend can be attributed to intra-group differences in terms of rastering velocity.

Figure 11. Characteristic scale comparison for polymeric scaffold bioprocessing methods and cardiovascular tissues.

Bioprocessing methods to produce polymeric scaffolds which mimic native tissue constituents and the relative characteristic scales. Electrospinning, double component deposition (DCD), jet spinning, melt electrowriting and two-photon polymerization enable the bioprocessing of the major constituents of the cardiovascular extracellular matrix: collagen and elastin. The current state of the art of cardiovascular tissue bioprocessing covers the entire scale range from sub-cellular to organ level with only one *iato* remaining between 10 and 100 nm.

Supplemental Figure 1. Methodology introduced to calculate scaffold AR. Schematic of the methodology used to calculate scaffold AR at a desired stress level that corresponds to the AR measured for native cardiovascular tissues. Step 1: scaffold specimens are tested under equi-stress biaxial conditions. Step 2: the AR is calculated at the four prescribed stress levels (11.0 kPa, 44.1 kPa, 220.5 kPa, 418.9 kPa allowed to cover the full range of physiologically relevant deformations for native cardiac tissue: stretch range = 1-1.3 (soft matter)) based on experimental data. Step 3: the experimentally derived scaffold ARs and their related stress values are linearly interpolated. Step 4: the AR vs. stress linear interpolation is utilized to estimate AR at the stress value that would

match the maximum stress utilized to elicit a specific physiologically relevant strain for the targeted cardiovascular tissue type.

References

1. Huang, Z.-M., et al., *A review on polymer nanofibers by electrospinning and their applications in nanocomposites*. Composites Science and Technology, 2003. **63**(15): p. 2223-2253.
2. D'Amore, A., et al., *Characterization of the complete fiber network topology of planar fibrous tissues and scaffolds*. Biomaterials, 2010. **31**(20): p. 5345-5354.
3. Li, W.-J., et al., *Fabrication and characterization of six electrospun poly(α -hydroxy ester)-based fibrous scaffolds for tissue engineering applications*. Acta Biomaterialia, 2006. **2**(4): p. 377-385.
4. Courtney, T., et al., *Design and analysis of tissue engineering scaffolds that mimic soft tissue mechanical anisotropy*. Biomaterials, 2006. **27**(19): p. 3631-3638.
5. Murugan, R. and S. Ramakrishna, *Design strategies of tissue engineering scaffolds with controlled fiber orientation*. Tissue engineering, 2007. **13**(8): p. 1845-1866.
6. Tsamis, A., et al., *Fiber micro-architecture in the longitudinal-radial and circumferential-radial planes of ascending thoracic aortic aneurysm media*. Journal of Biomechanics, 2013. **46**(16): p. 2787-2794.
7. Annabi, N., et al., *Controlling the porosity and microarchitecture of hydrogels for tissue engineering*. Tissue Engineering Part B: Reviews, 2010. **16**(4): p. 371-383.
8. D'Amore, A., et al., *Heart valve scaffold fabrication: Bioinspired control of macro-scale morphology, mechanics and micro-structure*. Biomaterials, 2018. **150**: p. 25-37.
9. Venugopal, J., et al., *Interaction of cells and nanofiber scaffolds in tissue engineering*. J Biomed Mater Res B Appl Biomater, 2008. **84**(1): p. 34-48.
10. Chen, M., et al., *Role of fiber diameter in adhesion and proliferation of NIH 3T3 fibroblast on electrospun polycaprolactone scaffolds*. Tissue Eng, 2007. **13**(3): p. 579-87.
11. Teo, W.E. and S. Ramakrishna, *A review on electrospinning design and nanofibre assemblies*. Nanotechnology, 2006. **17**(14): p. R89-R106.
12. Engelmayr, G.C., Jr. and M.S. Sacks, *A structural model for the flexural mechanics of nonwoven tissue engineering scaffolds*. J Biomech Eng, 2006. **128**(4): p. 610-22.
13. D'Amore, A., et al., *Meso-scale topological cues influence extracellular matrix production in a large deformation, elastomeric scaffold model*. Soft matter, 2018. **14**(42): p. 8483-8495.

14. Task, K., et al., *Systems level approach reveals the correlation of endoderm differentiation of mouse embryonic stem cells with specific microstructural cues of fibrin gels*. J R Soc Interface, 2014. **11**(95): p. 20140009.
15. Ambrosio, F., et al., *The effect of muscle loading on skeletal muscle regenerative potential: an update of current research findings relating to aging and neuromuscular pathology*. Am J Phys Med Rehabil, 2009. **88**(2): p. 145-55.
16. Wissing, T.B., et al., *Macrophage-Driven Biomaterial Degradation Depends on Scaffold Microarchitecture*. Frontiers in Bioengineering and Biotechnology, 2019. **7**(87).
17. Keane, T.J., et al., *Consequences of ineffective decellularization of biologic scaffolds on the host response*. Biomaterials, 2012. **33**(6): p. 1771-1781.
18. Amoroso, N.J., et al., *Microstructural manipulation of electrospun scaffolds for specific bending stiffness for heart valve tissue engineering*. Acta biomaterialia, 2012. **8**(12): p. 4268-4277.
19. Amoroso, N.J., et al., *Elastomeric electrospun polyurethane scaffolds: the interrelationship between fabrication conditions, fiber topology, and mechanical properties*. Advanced Materials, 2011. **23**(1): p. 106-111.
20. Hasan, A., et al., *Biomechanical properties of native and tissue engineered heart valve constructs*. J Biomech, 2014. **47**(9): p. 1949-63.
21. Loerakker, S., et al., *Effects of valve geometry and tissue anisotropy on the radial stretch and coaptation area of tissue-engineered heart valves*. J Biomech, 2013. **46**(11): p. 1792-800.
22. Schoen, F.J., *Evolving concepts of cardiac valve dynamics: the continuum of development, functional structure, pathobiology, and tissue engineering*. Circulation, 2008. **118**(18): p. 1864-1880.
23. Masoumi, N., et al., *Tri-layered elastomeric scaffolds for engineering heart valve leaflets*. Biomaterials, 2014. **35**(27): p. 7774-7785.
24. Ho, S.Y., *Anatomy and myoarchitecture of the left ventricular wall in normal and in disease*. European Journal of Echocardiography, 2009. **10**(8): p. iii3-iii7.
25. Bian, W., C.P. Jackman, and N. Bursac, *Controlling the structural and functional anisotropy of engineered cardiac tissues*. Biofabrication, 2014. **6**(2): p. 024109.
26. Lillie, M., R. Shadwick, and J. Gosline, *Mechanical anisotropy of inflated elastic tissue from the pig aorta*. Journal of biomechanics, 2010. **43**(11): p. 2070-2078.
27. Wolinsky, H. and S. Glagov, *Structural basis for the static mechanical properties of the aortic media*. Circulation research, 1964. **14**(5): p. 400-413.

28. Hashizume, R., et al., *Morphological and mechanical characteristics of the reconstructed rat abdominal wall following use of a wet electrospun biodegradable polyurethane elastomer scaffold*. *Biomaterials*, 2010. **31**(12): p. 3253-3265.
29. Hong, Y., et al., *Mechanical properties and in vivo behavior of a biodegradable synthetic polymer microfiber-extracellular matrix hydrogel biohybrid scaffold*. *Biomaterials*, 2011. **32**(13): p. 3387-3394.
30. Guan, J., et al., *Synthesis, characterization, and cytocompatibility of elastomeric, biodegradable poly (ester-urethane) ureas based on poly (caprolactone) and putrescine*. *Journal of Biomedical Materials Research: An Official Journal of The Society for Biomaterials, The Japanese Society for Biomaterials, and The Australian Society for Biomaterials and the Korean Society for Biomaterials*, 2002. **61**(3): p. 493-503.
31. Ayres, C., et al., *Modulation of anisotropy in electrospun tissue-engineering scaffolds: Analysis of fiber alignment by the fast Fourier transform*. *Biomaterials*, 2006. **27**(32): p. 5524-5534.
32. Li, W.-J., et al., *Engineering controllable anisotropy in electrospun biodegradable nanofibrous scaffolds for musculoskeletal tissue engineering*. *Journal of biomechanics*, 2007. **40**(8): p. 1686-1693.
33. Sacks, M.S., *Biaxial mechanical evaluation of planar biological materials*. *Journal of elasticity and the physical science of solids*, 2000. **61**(1-3): p. 199.
34. D'Amore, A., et al., *From single fiber to macro-level mechanics: a structural finite-element model for elastomeric fibrous biomaterials*. *Journal of the mechanical behavior of biomedical materials*, 2014. **39**: p. 146-161.
35. Guccione, J.M., A.D. McCulloch, and L.K. Waldman, *Passive material properties of intact ventricular myocardium determined from a cylindrical model*. *J Biomech Eng*, 1991. **113**(1): p. 42-55.
36. Holmes, J.W., T.K. Borg, and J.W. Covell, *Structure and mechanics of healing myocardial infarcts*. *Annu. Rev. Biomed. Eng.*, 2005. **7**: p. 223-253.
37. Sacks, M.S., et al., *Surface Strains in the Anterior Leaflet of the Functioning Mitral Valve*. *Annals of Biomedical Engineering*, 2002. **30**(10): p. 1281-1290.
38. Human, P., et al., *Decellularization and engineered crosslinking: a promising dual approach towards bioprosthetic heart valve longevity*. *Eur J Cardiothorac Surg*, 2020. **58**(6): p. 1192-1200.
39. Stankus, J.J., et al., *Fabrication of cell microintegrated blood vessel constructs through electrohydrodynamic atomization*. *Biomaterials*, 2007. **28**(17): p. 2738-2746.

40. Kamenskiy, A.V., et al., *Comparative analysis of the biaxial mechanical behavior of carotid wall tissue and biological and synthetic materials used for carotid patch angioplasty*. Journal of biomechanical engineering, 2011. **133**(11): p. 111008.
41. Kamenskiy, A.V., et al., *Passive biaxial mechanical properties and in vivo axial pre-stretch of the diseased human femoropopliteal and tibial arteries*. Acta biomaterialia, 2014. **10**(3): p. 1301-1313.
42. Sánchez-Palencia, D.M., et al., *Effects of fabrication on the mechanics, microstructure and micromechanical environment of small intestinal submucosa scaffolds for vascular tissue engineering*. Journal of Biomechanics, 2014. **47**(11): p. 2766-2773.
43. Soleimanifard, S., et al., *Three-dimensional regional strain analysis in porcine myocardial infarction: a 3T magnetic resonance tagging study*. Journal of Cardiovascular Magnetic Resonance, 2012. **14**(1): p. 1-12.
44. Yuda, S., et al., *Quantitative measurement of circumferential carotid arterial strain by two-dimensional speckle tracking imaging in healthy subjects*. Echocardiography, 2011. **28**(8): p. 899-906.
45. Yuda, S., et al., *Quantitative measurement of circumferential carotid arterial strain by two-dimensional speckle tracking imaging in healthy subjects*. Echocardiography, 2011. **28**(8): p. 899-906.
46. Matsumura, Y., et al., *Intramyocardial injection of a fully synthetic hydrogel attenuates left ventricular remodeling post myocardial infarction*. Biomaterials, 2019: p. 119289.
47. Murdock, M.H., et al., *Cytocompatibility and mechanical properties of surgical sealants for cardiovascular applications*. The Journal of thoracic and cardiovascular surgery, 2019. **157**(1): p. 176-183.
48. Chauduri, B., P. Kundo, and S. Nirupam, *Detection and gradation of oriented texture*. Pattern Recogn Lett, 1993. **14**: p. 147-153.
49. Agoram, B. and V.H. Barocas, *Coupled macroscopic and microscopic scale modeling of fibrillar tissues and tissue equivalents*. J Biomech Eng, 2001. **123**(4): p. 362-9.
50. Sacks, M.S. and C.J. Chuong, *Characterization of collagen fiber architecture in the canine diaphragmatic central tendon*. J Biomech Eng, 1992. **114**(2): p. 183-90.
51. Takanari, K., et al., *Abdominal wall reconstruction by a regionally distinct biocomposite of extracellular matrix digest and a biodegradable elastomer*. J Tissue Eng Regen Med, 2016. **10**(9): p. 748-61.
52. Saily, N.T., et al., *Biologically inspired scaffolds for heart valve tissue engineering via melt electrowriting*. Small, 2019. **15**(24): p. 1900873.

53. Badrossamay, M.R., et al., *Engineering hybrid polymer-protein super-aligned nanofibers via rotary jet spinning*. Biomaterials, 2014. **35**(10): p. 3188-3197.
54. Rutledge, G.C. and S.V. Fridrikh, *Formation of fibers by electrospinning*. Advanced drug delivery reviews, 2007. **59**(14): p. 1384-1391.
55. Stella, J.A., et al., *Tissue-to-cellular level deformation coupling in cell micro-integrated elastomeric scaffolds*. Biomaterials, 2008. **29**(22): p. 3228-3236.
56. Driessen, N.J., et al., *Modeling the mechanics of tissue-engineered human heart valve leaflets*. Journal of biomechanics, 2007. **40**(2): p. 325-334.
57. van Kelle, M., et al., *Initial scaffold thickness affects the emergence of a geometrical and mechanical equilibrium in engineered cardiovascular tissues*. Journal of the Royal Society Interface, 2018. **15**(148): p. 20180359.
58. Hasan, A., et al., *Biomechanical properties of native and tissue engineered heart valve constructs*. Journal of biomechanics, 2014. **47**(9): p. 1949-1963.
59. Engelmayer, G.C., et al., *Accordion-like honeycombs for tissue engineering of cardiac anisotropy*. Nature materials, 2008. **7**(12): p. 1003-1010.
60. Syedain, Z.H., et al., *Implantable arterial grafts from human fibroblasts and fibrin using a multi-graft pulsed flow-stretch bioreactor with noninvasive strength monitoring*. Biomaterials, 2011. **32**(3): p. 714-722.
61. Soletti, L., et al., *A bilayered elastomeric scaffold for tissue engineering of small diameter vascular grafts*. Acta biomaterialia, 2010. **6**(1): p. 110-122.
62. Vaz, C., et al., *Design of scaffolds for blood vessel tissue engineering using a multi-layering electrospinning technique*. Acta biomaterialia, 2005. **1**(5): p. 575-582.
63. Sill, T.J. and H.A. von Recum, *Electrospinning: applications in drug delivery and tissue engineering*. Biomaterials, 2008. **29**(13): p. 1989-2006.
64. Xu, C., et al., *Electrospun nanofiber fabrication as synthetic extracellular matrix and its potential for vascular tissue engineering*. Tissue engineering, 2004. **10**(7-8): p. 1160-1168.
65. Yokoyama, Y., et al., *Novel wet electrospinning system for fabrication of spongiform nanofiber 3-dimensional fabric*. Materials letters, 2009. **63**(9-10): p. 754-756.
66. Mela, P. and A. D'Amore, *In Situ Heart Valve Tissue Engineering: Is Scaffold Structural Biomimicry Overrated?* 2020, American College of Cardiology Foundation Washington DC.
67. Hobson, C.M., et al., *Fabrication of elastomeric scaffolds with curvilinear fibrous structures for heart valve leaflet engineering*. Journal of Biomedical Materials Research Part A, 2015. **103**(9): p. 3101-3106.

68. Bisht, G.S., et al., *Controlled continuous patterning of polymeric nanofibers on three-dimensional substrates using low-voltage near-field electrospinning*. Nano letters, 2011. **11**(4): p. 1831-1837.
69. Cramariuc, B., et al., *Fiber diameter in electrospinning process*. Journal of Electrostatics, 2013. **71**(3): p. 189-198.
70. Thompson, C., et al., *Effects of parameters on nanofiber diameter determined from electrospinning model*. Polymer, 2007. **48**(23): p. 6913-6922.
71. Boublik, J., et al., *Mechanical properties and remodeling of hybrid cardiac constructs made from heart cells, fibrin, and biodegradable, elastomeric knitted fabric*. Tissue Engineering, 2005. **11**(7-8): p. 1122-1132.
72. Dalton, P.D., *Melt electrowriting with additive manufacturing principles*. Current Opinion in Biomedical Engineering, 2017. **2**: p. 49-57.
73. Kim, J.Y., et al., *Design of a modified electrospinning for the in-situ fabrication of 3D cotton-like collagen fiber bundle mimetic scaffold*. Materials Letters, 2019. **236**: p. 521-525.
74. Li, W.-J., et al., *Fabrication and characterization of six electrospun poly (α -hydroxy ester)-based fibrous scaffolds for tissue engineering applications*. Acta biomaterialia, 2006. **2**(4): p. 377-385.
75. Mattila, P.K. and P. Lappalainen, *Filopodia: molecular architecture and cellular functions*. Nature reviews Molecular cell biology, 2008. **9**(6): p. 446-454.
76. Okorokov, A.L., et al., *Structure of the hDmc1-ssDNA filament reveals the principles of its architecture*. PloS one, 2010. **5**(1): p. e8586.
77. Raimondi, M.T., et al., *Two-photon laser polymerization: from fundamentals to biomedical application in tissue engineering and regenerative medicine*. Journal of applied biomaterials & functional materials, 2012. **10**(1): p. 56-66.
78. Stephanopoulos, N., J.H. Ortony, and S.I. Stupp, *Self-assembly for the synthesis of functional biomaterials*. Acta materialia, 2013. **61**(3): p. 912-930.
79. Thubrikar, M.J., *Vascular mechanics and pathology*. Vol. 494. 2007: Springer.
80. Ushiki, T., *Collagen fibers, reticular fibers and elastic fibers. A comprehensive understanding from a morphological viewpoint*. Archives of histology and cytology, 2002. **65**(2): p. 109-126.
81. Yang, S., et al., *The design of scaffolds for use in tissue engineering. Part II. Rapid prototyping techniques*. Tissue engineering, 2002. **8**(1): p. 1-11.

Table 1. Electrospun scaffold thickness

Fabrication conditions		Thickness (mm)			
Vr (cm/s)	Vt (m/s)	Dry		Wet	
		Avg	SE	Avg	SE
0.16	0.3	0.134	0.022	0.151	0.011
0.16	1.5	0.077	0.011	0.050	0.004
0.16	3.0	0.087	0.002	0.075	0.006
0.16	4.5	0.148	0.005	0.084	0.002
0.16	9.0	0.211	0.004	0.105	0.002
2.5	0.3	0.072	0.005	0.077	0.002
2.5	1.5	0.080	0.015	0.052	0.002
2.5	3.0	0.098	0.005	0.109	0.003
2.5	4.5	0.051	0.001	0.102	0.001
2.5	9.0	0.142	0.003	0.049	0.003
8.0	0.3	0.066	0.001	0.032	0.001
8.0	1.5	0.048	0.002	0.039	0.001
8.0	3.0	0.077	0.001	0.089	0.014
8.0	4.5	0.105	0.002	0.072	0.005
8.0	9.0	0.108	0.002	0.062	0.001

Table 2. Native porcine cardiac tissue anisotropy

Tissue Specimen	Peak stress (kPa)	Anisotropy Ratio
Left Ventricle	5.3	1.043
Aortic Valve	44.1	1.159
Mitral Valve	44.1	1.078
Pulmonic Valve	44.1	1.182
Tricuspid Valve	44.1	1.082
Carotid Artery	54.0	1.101
Descending Aorta	54.0	1.047

Table 3. Circumferential, longitudinal and total strain energy of native cardiovascular tissues presented as average and standard error. Number of samples (n) is reported.

Strain Energy (kJ)	Circ. Direction		Long. Direction		Total		n
	AVG	SE	AVG	SE	AVG	SE	
Left Ventricle	0.30	0.05	0.53	0.07	0.83	0.11	3
Aortic Valve	4.92	1.09	20.93	3.34	25.85	2.99	9
Mitral Valve	7.32	1.33	10.05	1.70	17.36	1.90	10
Pulmonary Valve	6.23	1.57	30.65	3.47	36.88	3.25	10
Tricuspid Valve	7.55	1.03	17.56	1.68	25.33	2.08	9
Carotid Artery	29.39	1.55	14.34	1.54	43.73	2.55	5
Descending Aorta	17.18	0.72	13.53	0.73	30.71	0.65	7

Table 4. Anisotropy ratio calculations for five stress values

Dry Fabrication

Translational Vel. (cm/s)	Tangential Vel. (m/s)	R ²	Equation
0.16	0.3	0.921	AR=-0.3x10 ⁻⁴ *(stress)+0.99924
	1.5	0.994	AR=1.0x10 ⁻⁴ *(stress)+0.99904
	3.0	0.979	AR=1.7x10 ⁻⁴ *(stress)+1.00890
	4.5	0.966	AR=3.8x10 ⁻⁴ *(stress)+1.02375
	9.0	0.945	AR=7.3x10 ⁻⁴ *(stress)+1.16136
2.5	0.3	0.919	AR=-1.0x10 ⁻⁴ *(stress)+0.99523
	1.5	0.949	AR=-0.4x10 ⁻⁴ *(stress)+1.00123
	3.0	0.958	AR=1.8x10 ⁻⁴ *(stress)+1.01894
	4.5	0.948	AR=2.5x10 ⁻⁴ *(stress)+1.01765
	9.0	0.937	AR=10.0x10 ⁻⁴ *(stress)+1.16873
8.0	0.3	0.979	AR=-0.4x10 ⁻⁴ *(stress)+0.99714
	1.5	0.970	AR=1.0x10 ⁻⁴ *(stress)+1.00006
	3.0	0.946	AR=4.1x10 ⁻⁴ *(stress)+1.04190
	4.5	0.958	AR=4.8x10 ⁻⁴ *(stress)+1.04553
	9.0	0.922	AR=13.7x10 ⁻⁴ *(stress)+1.29317

Wet Fabrication

Translational Vel. (cm/s)	Tangential Vel. (m/s)	R ²	Equation
0.16	0.3	0.853	AR=-0.3x10 ⁻⁴ *(stress)+0.99678
	1.5	0.909	AR=-0.2x10 ⁻⁴ *(stress)+1.00180
	3.0	0.973	AR=0.8x10 ⁻⁴ *(stress)+1.00618
	4.5	0.929	AR=3.3x10 ⁻⁴ *(stress)+1.02716
	9.0	0.903	AR=11.1x10 ⁻⁴ *(stress)+1.19433
2.5	0.3	0.994	AR=-0.9x10 ⁻⁴ *(stress)+0.99725
	1.5	0.933	AR=-0.3x10 ⁻⁴ *(stress)+1.00610
	3.0	0.825	AR=-0.2x10 ⁻⁴ *(stress)+1.00369
	4.5	0.998	AR=1.4x10 ⁻⁴ *(stress)+1.00161
	9.0	0.939	AR=12.1x10 ⁻⁴ *(stress)+1.15337
8.0	0.3	0.976	AR=-0.7x10 ⁻⁴ *(stress)+0.99293
	1.5	0.969	AR=-0.8x10 ⁻⁴ *(stress)+0.99891
	3.0	0.677	AR=-0.1x10 ⁻⁴ *(stress)+0.99797
	4.5	0.990	AR=1.8x10 ⁻⁴ *(stress)+0.99994
	9.0	0.946	AR=9.0x10 ⁻⁴ *(stress)+1.06297

TABLE 4

Table 5. Linear regression model

	Fabrication Conditions	R^2	C_0	a_1	a_2
Ventricle Wall	Dry	0.959	0.9844	0.0021	0.0016
	Wet	0.959	0.9972	0.0024	-0.0015
Heart Valve Leaflets	Dry	0.968	0.9847	0.0025	0.0019
	Wet	0.971	0.9944	0.0029	-0.0016
Large Blood Vessels	Dry	0.970	0.9848	0.0026	0.0019
	Wet	0.973	0.9937	0.0031	-0.0016

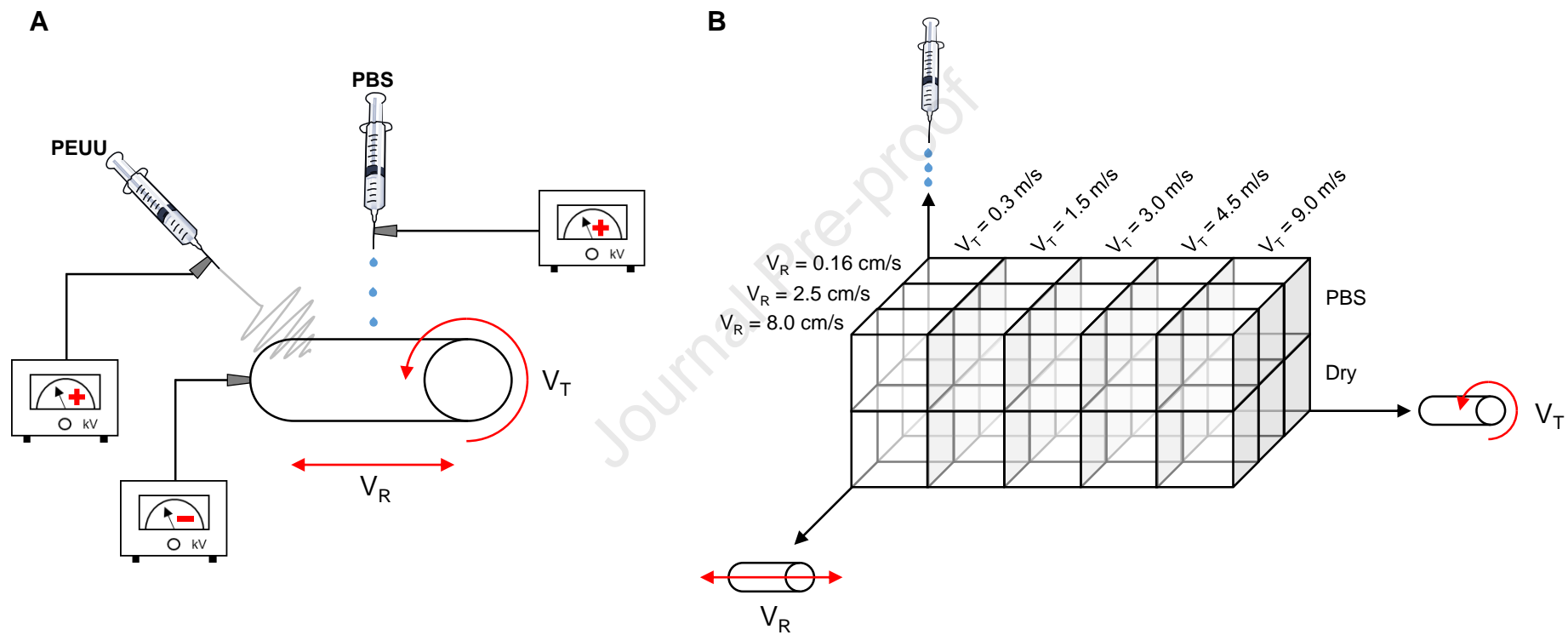
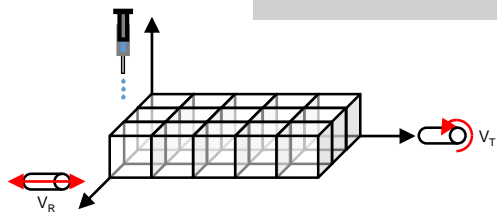


FIGURE 1

Dry Fabrication



Tangential Velocity

Rastering Velocity

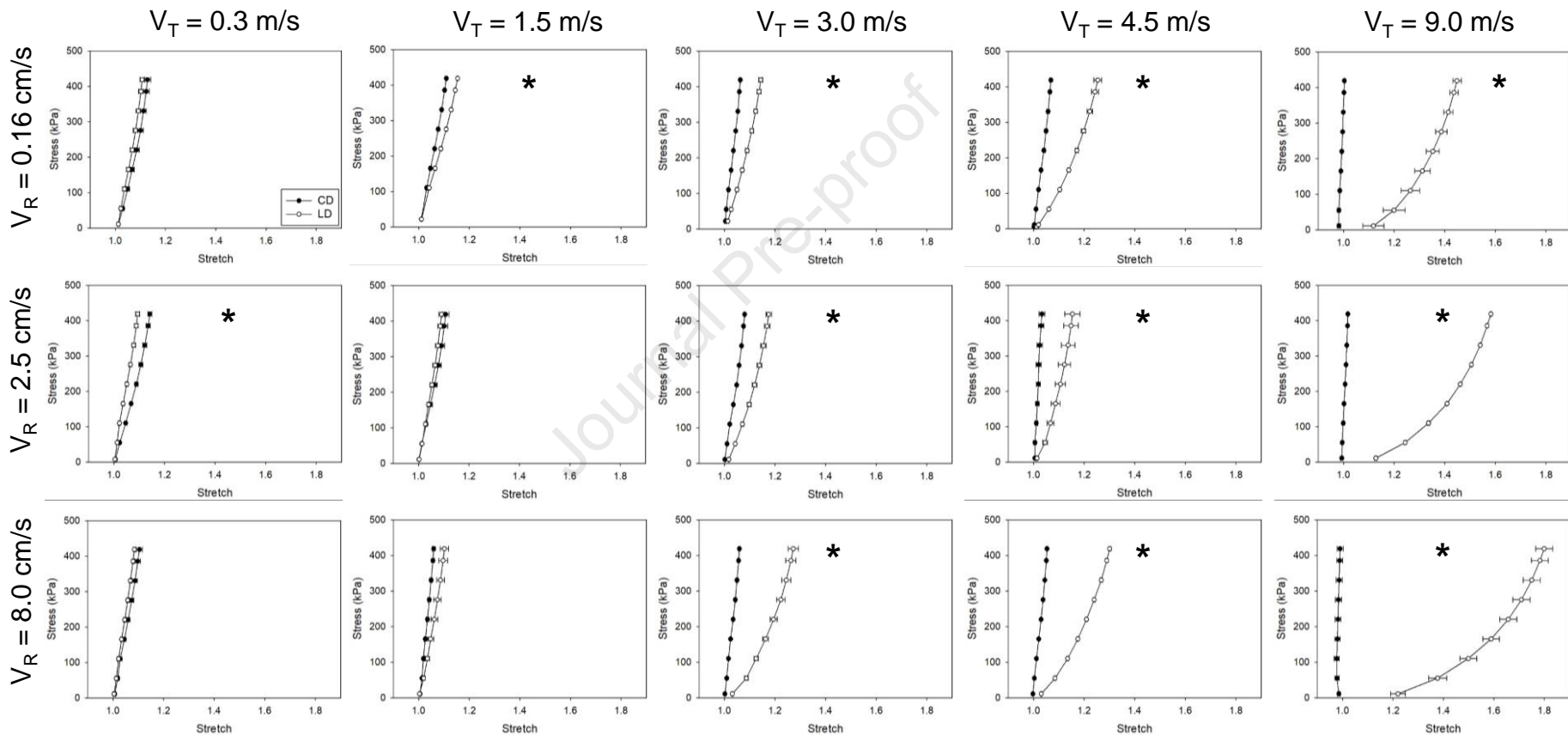
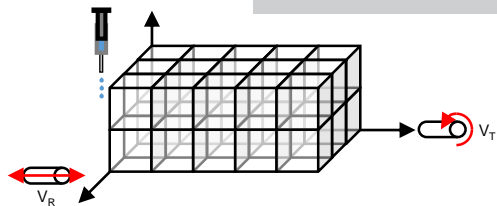


FIGURE 2

Wet Fabrication



Tangential Velocity

Rastering Velocity

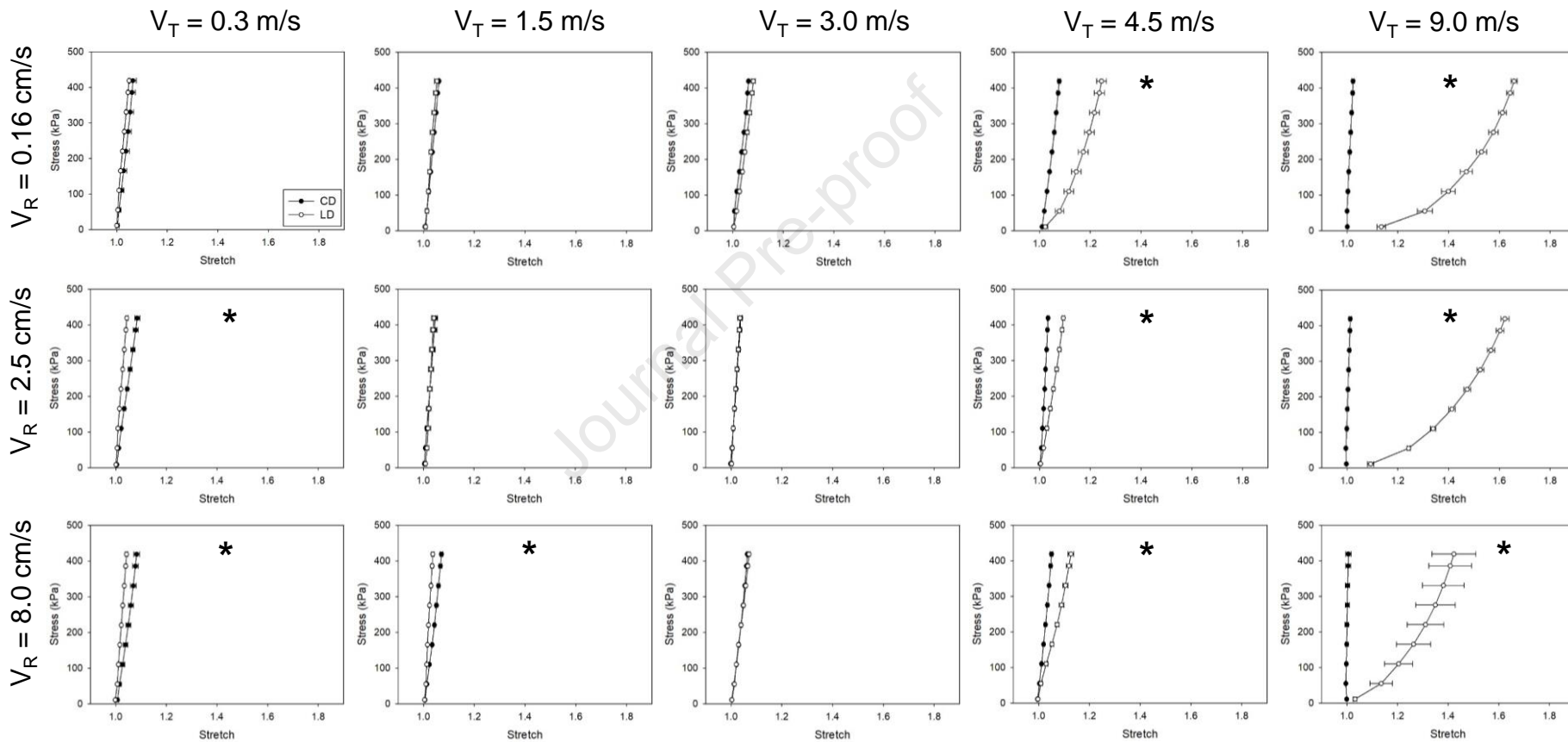
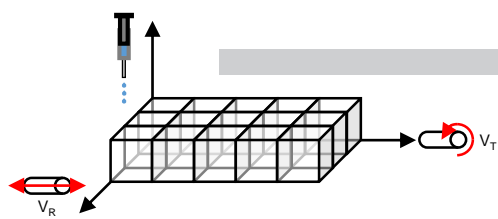
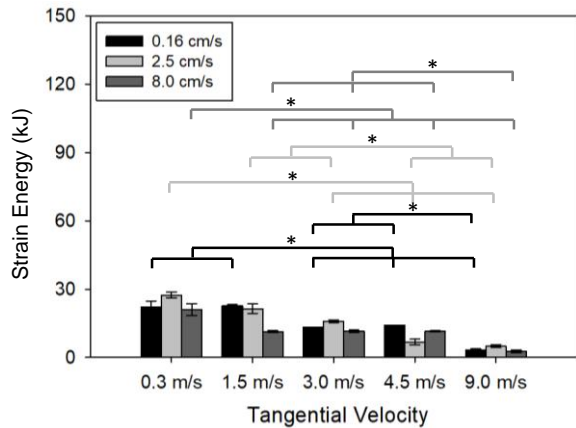


FIGURE 3

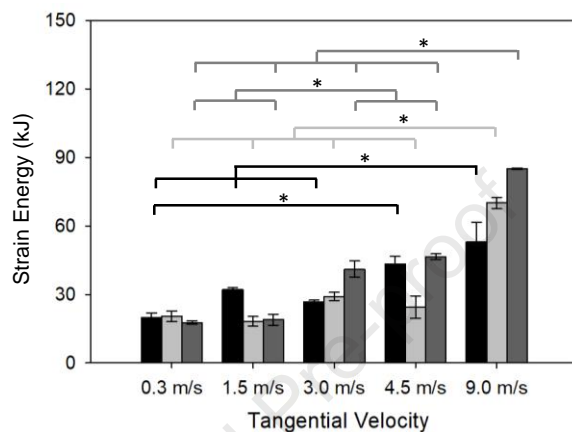
A



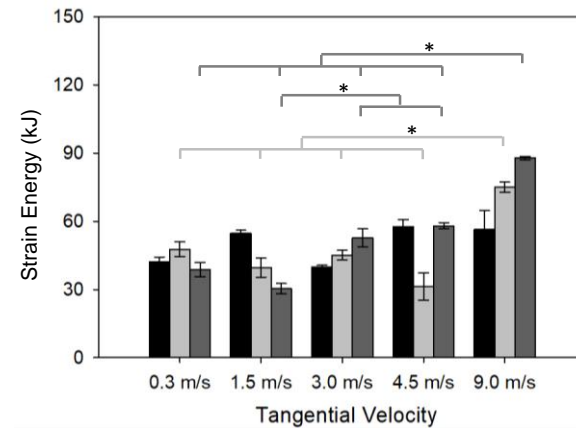
Circumferential Direction



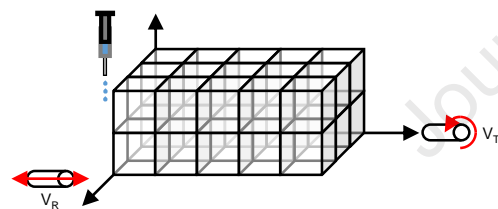
Longitudinal Direction



Total

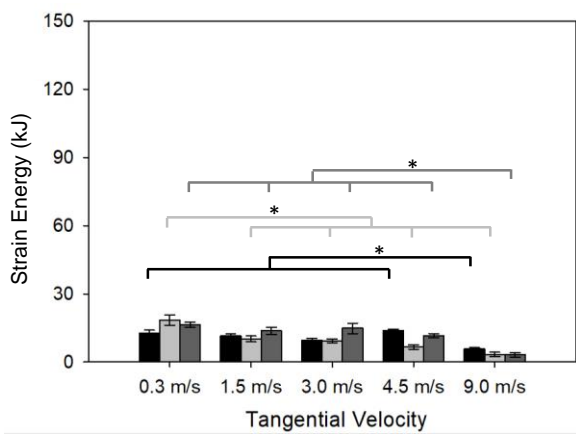


B

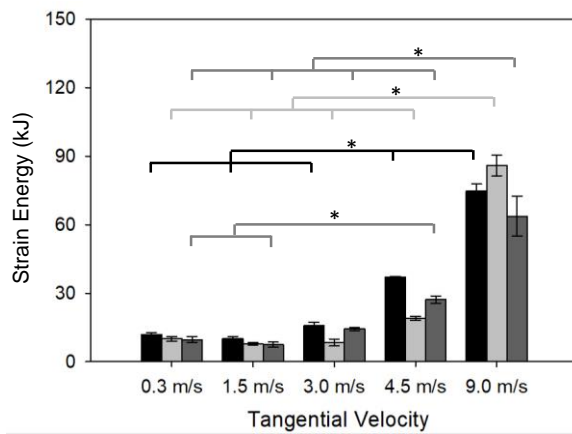


Wet Fabrication

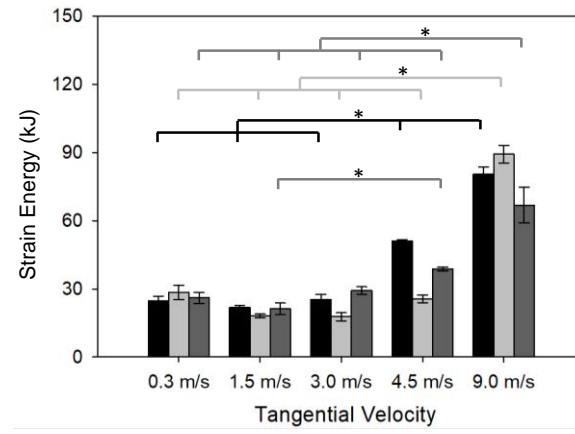
Circumferential Direction



Longitudinal Direction



Total



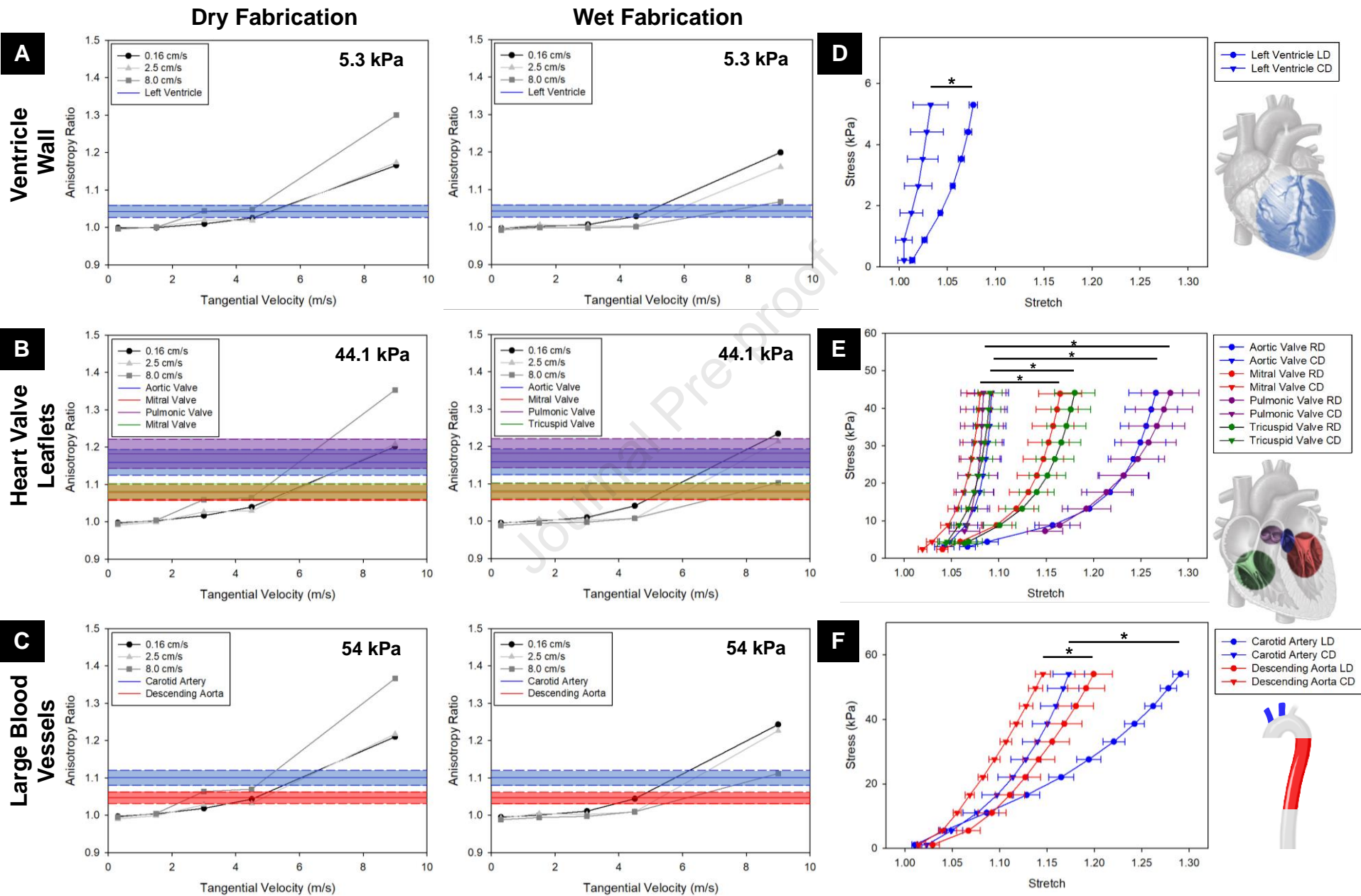
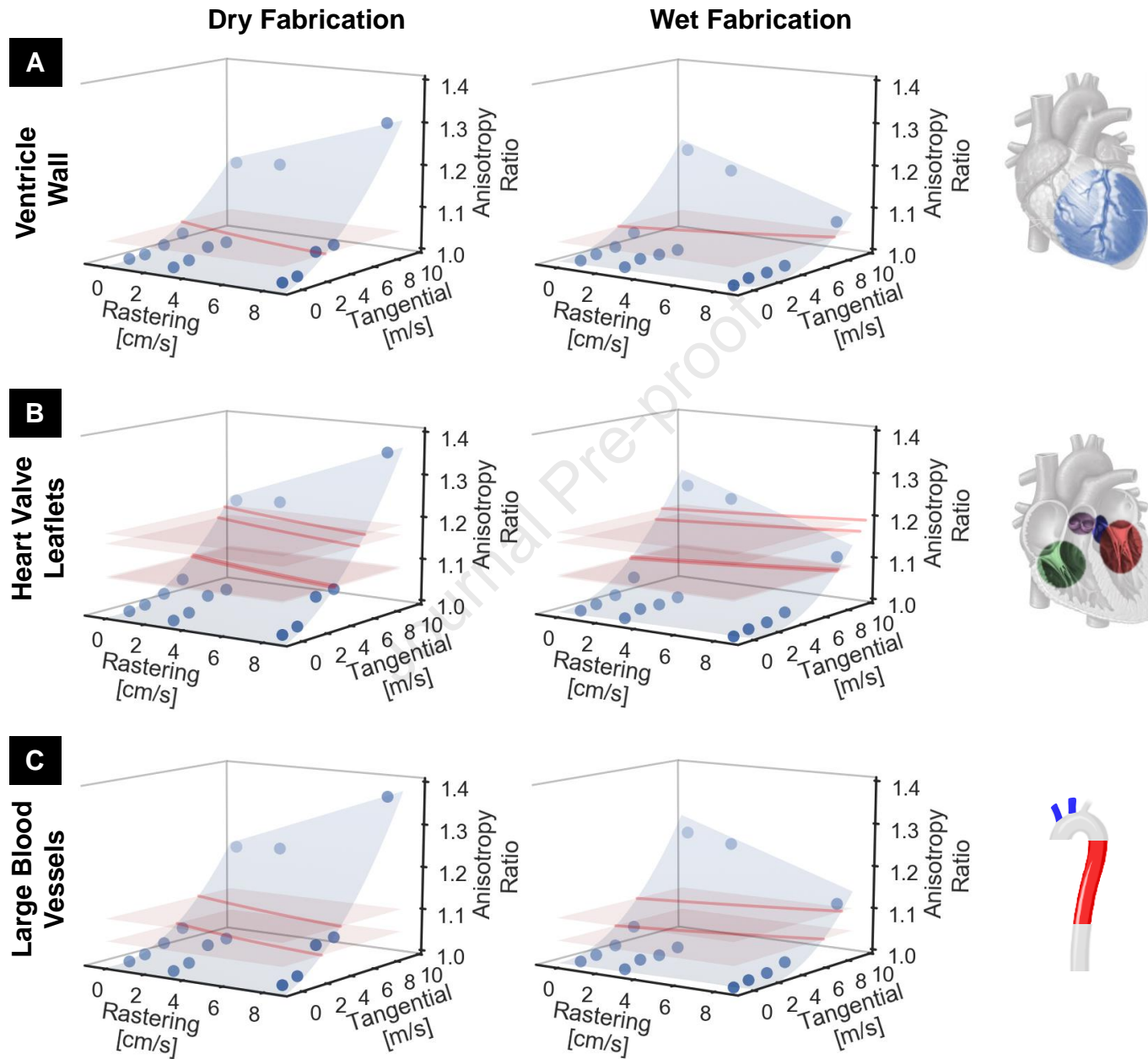
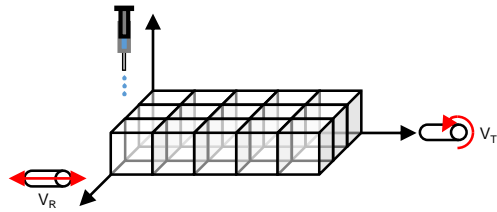


FIGURE 5

**FIGURE 6**



Dry Fabrication

Tangential Velocity

 $V_T = 0.3 \text{ m/s}$ $V_T = 1.5 \text{ m/s}$ $V_T = 3.0 \text{ m/s}$ $V_T = 4.5 \text{ m/s}$ $V_T = 9.0 \text{ m/s}$

Rastering Velocity

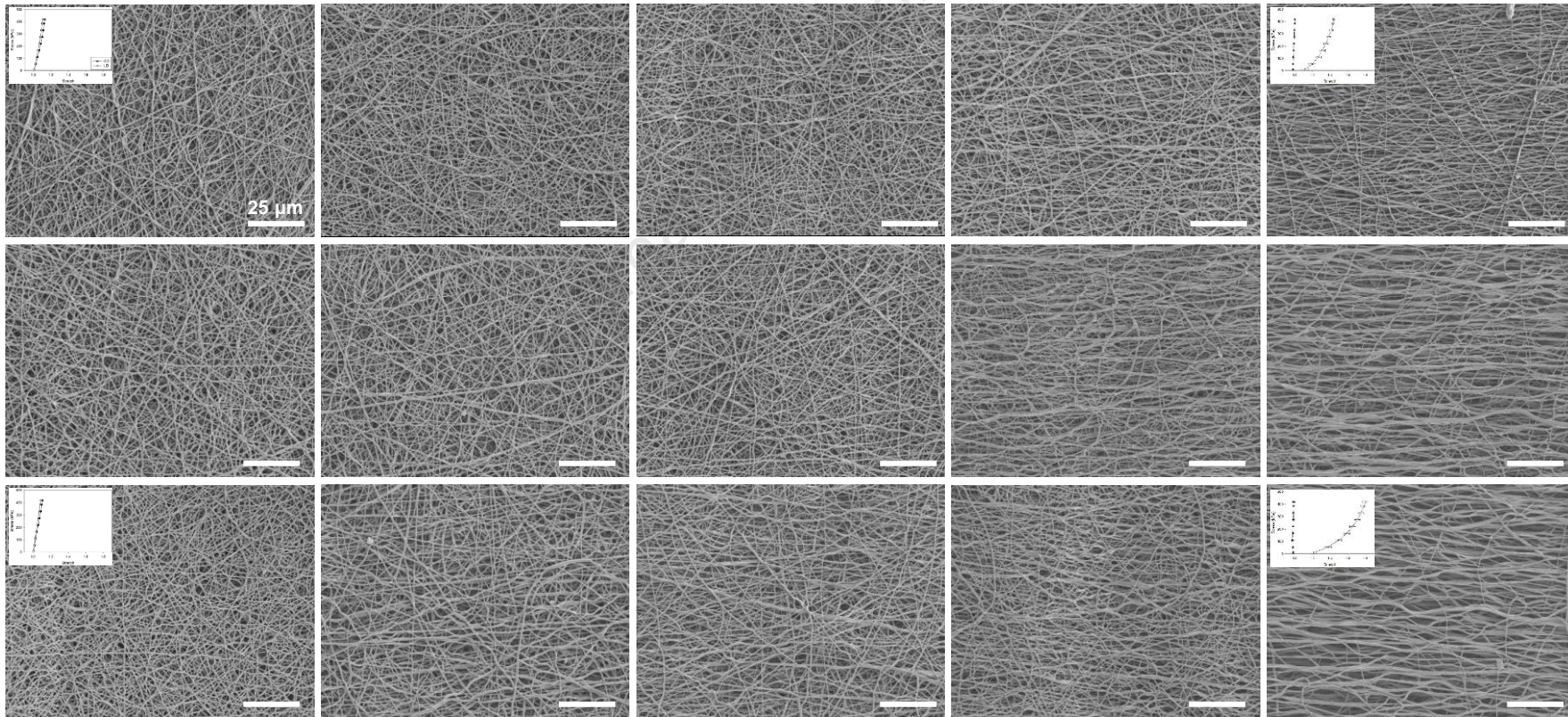
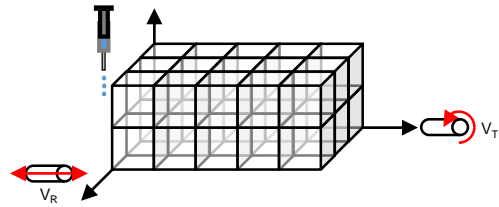
 $V_R = 0.16 \text{ cm/s}$ $V_R = 2.5 \text{ cm/s}$ $V_R = 8.0 \text{ cm/s}$ 

FIGURE 7



Wet Fabrication

Tangential Velocity

 $V_T = 0.3 \text{ m/s}$ $V_T = 1.5 \text{ m/s}$ $V_T = 3.0 \text{ m/s}$ $V_T = 4.5 \text{ m/s}$ $V_T = 9.0 \text{ m/s}$

Rasting Velocity

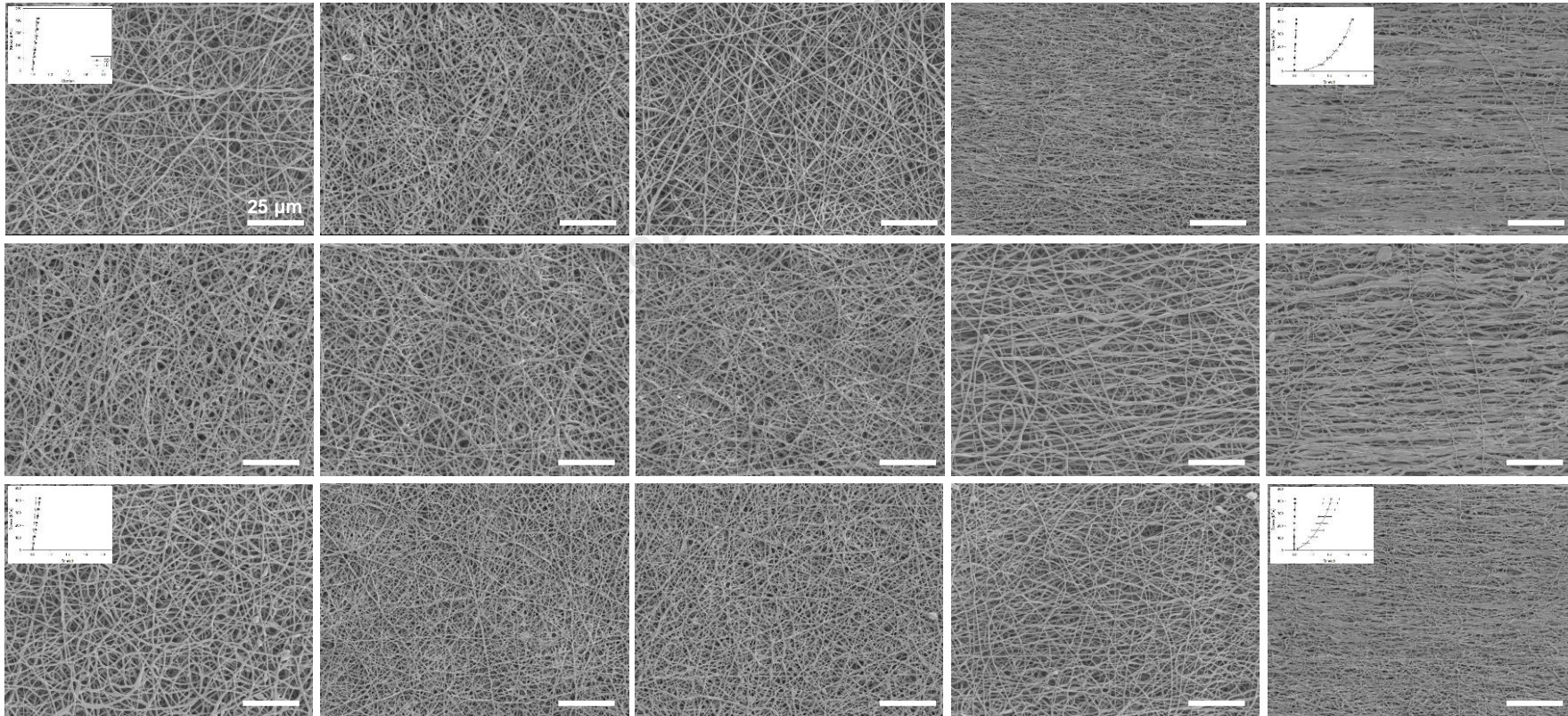
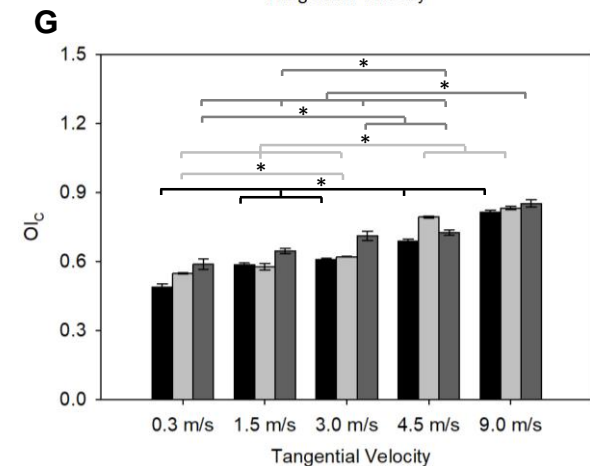
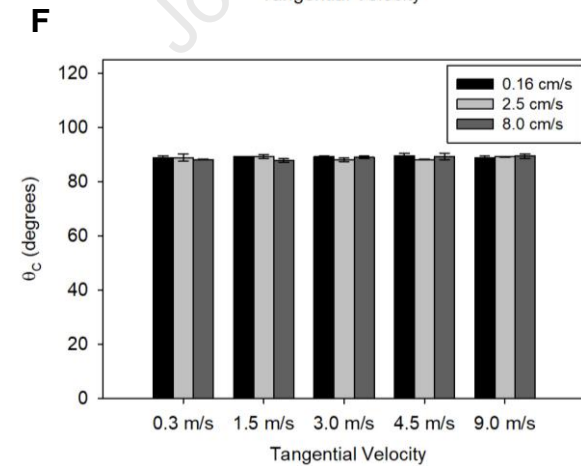
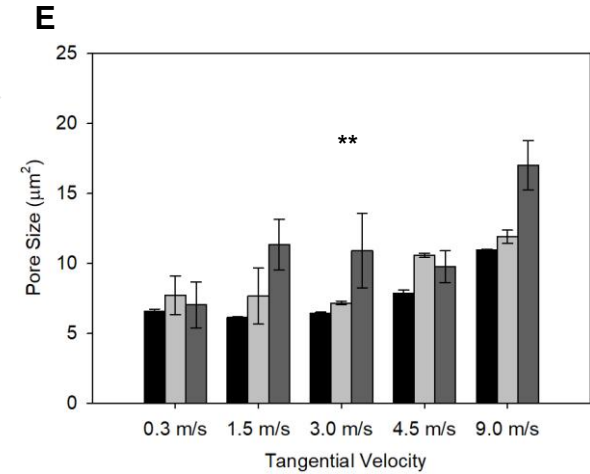
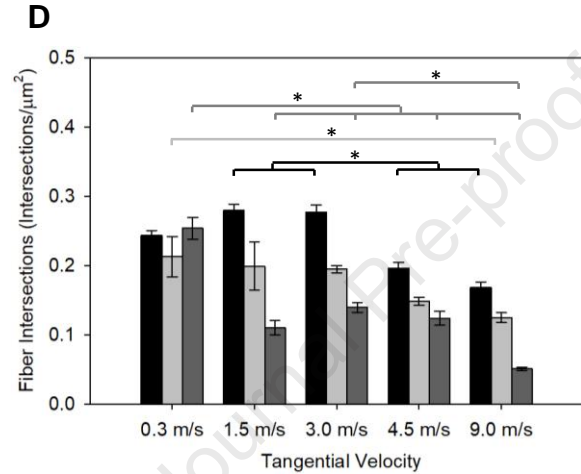
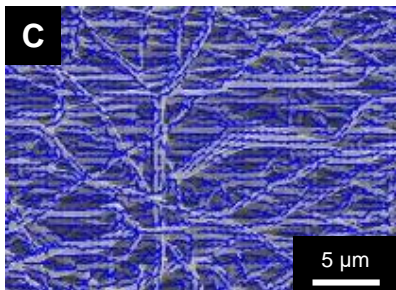
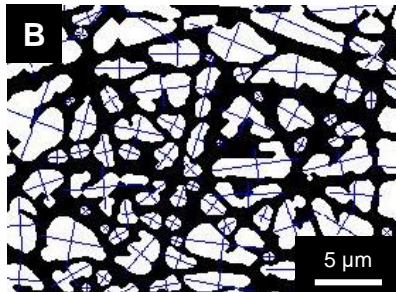
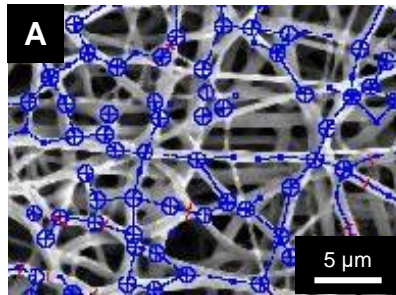
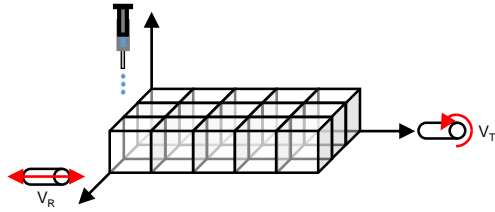
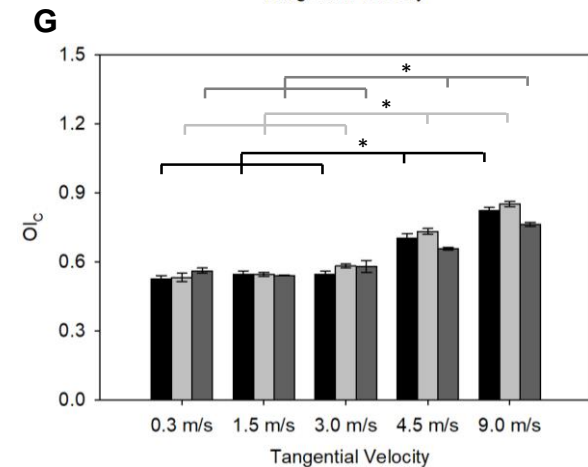
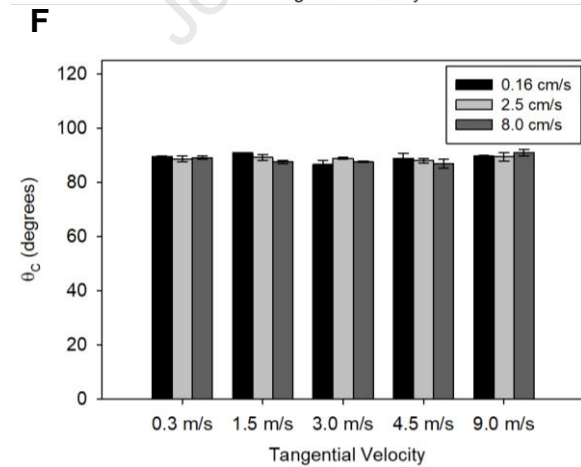
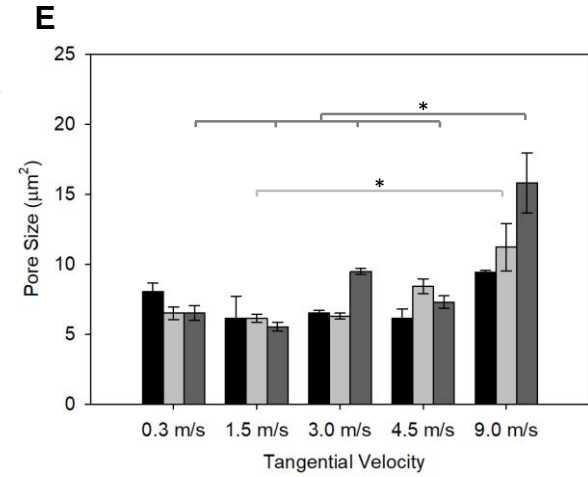
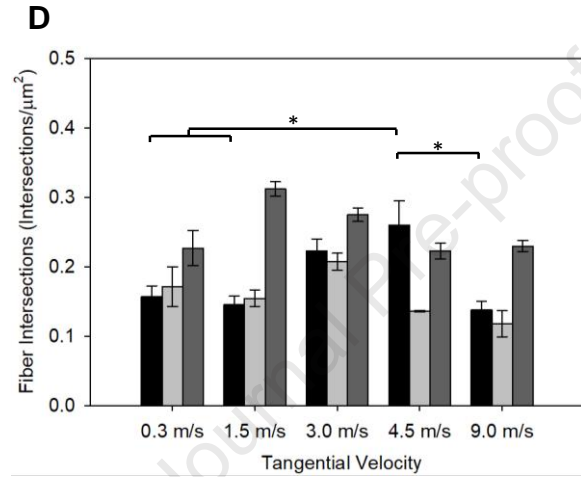
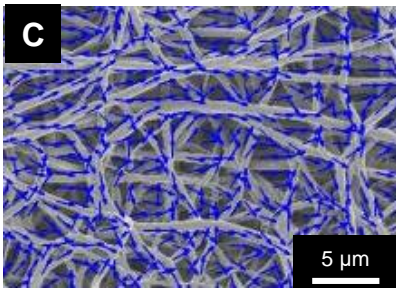
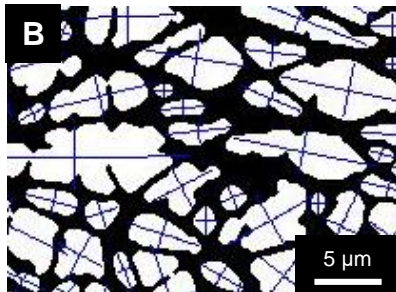
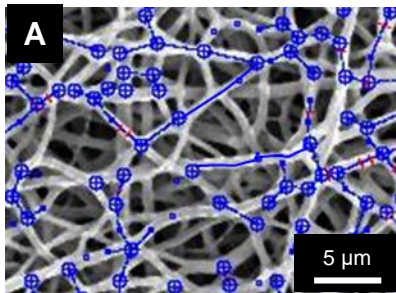
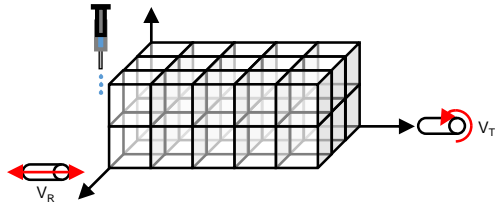
 $V_R = 0.16 \text{ cm/s}$ $V_R = 2.5 \text{ cm/s}$ $V_R = 8.0 \text{ cm/s}$ 

FIGURE 8

Dry Fabrication



Wet Fabrication



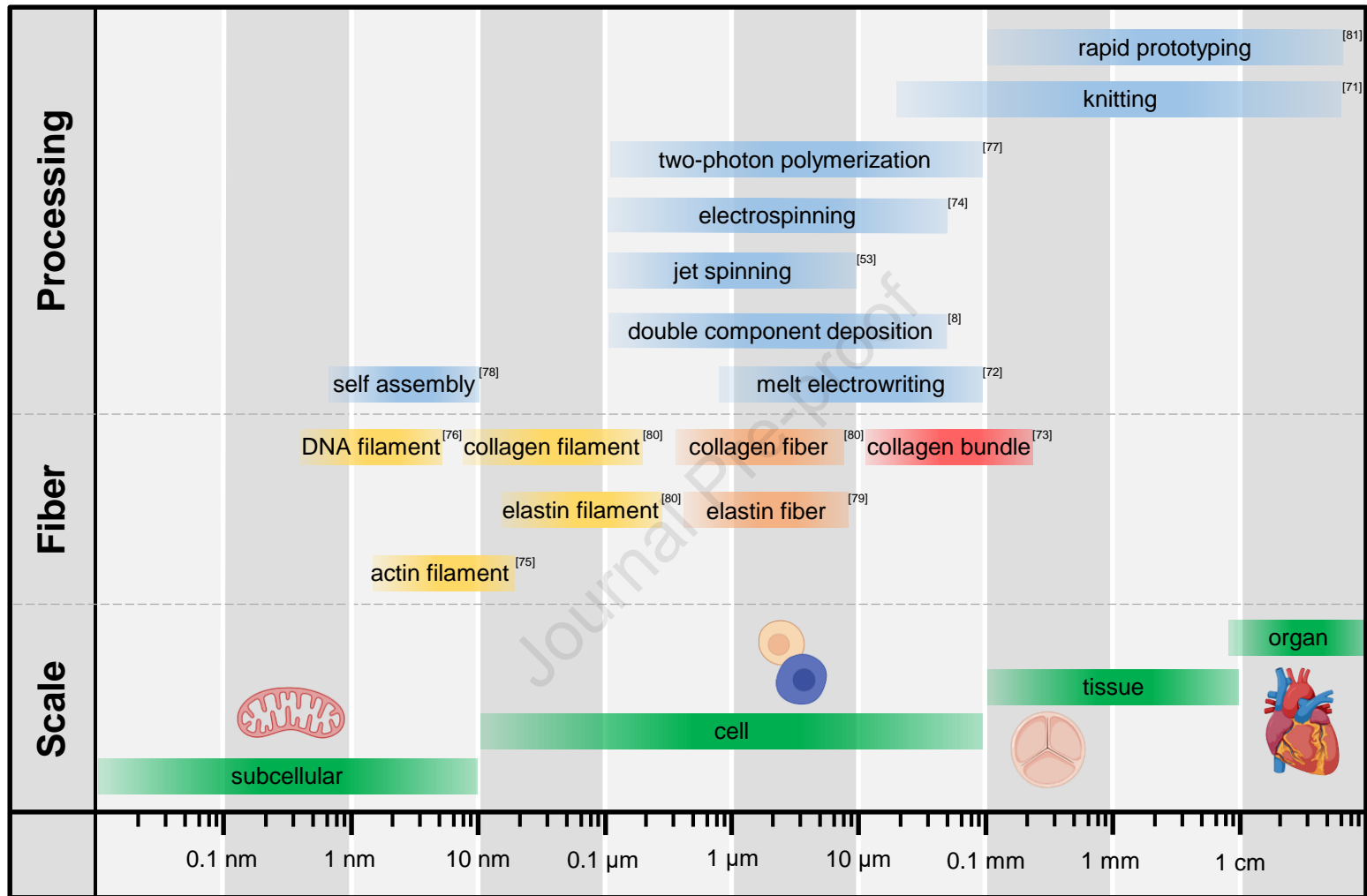
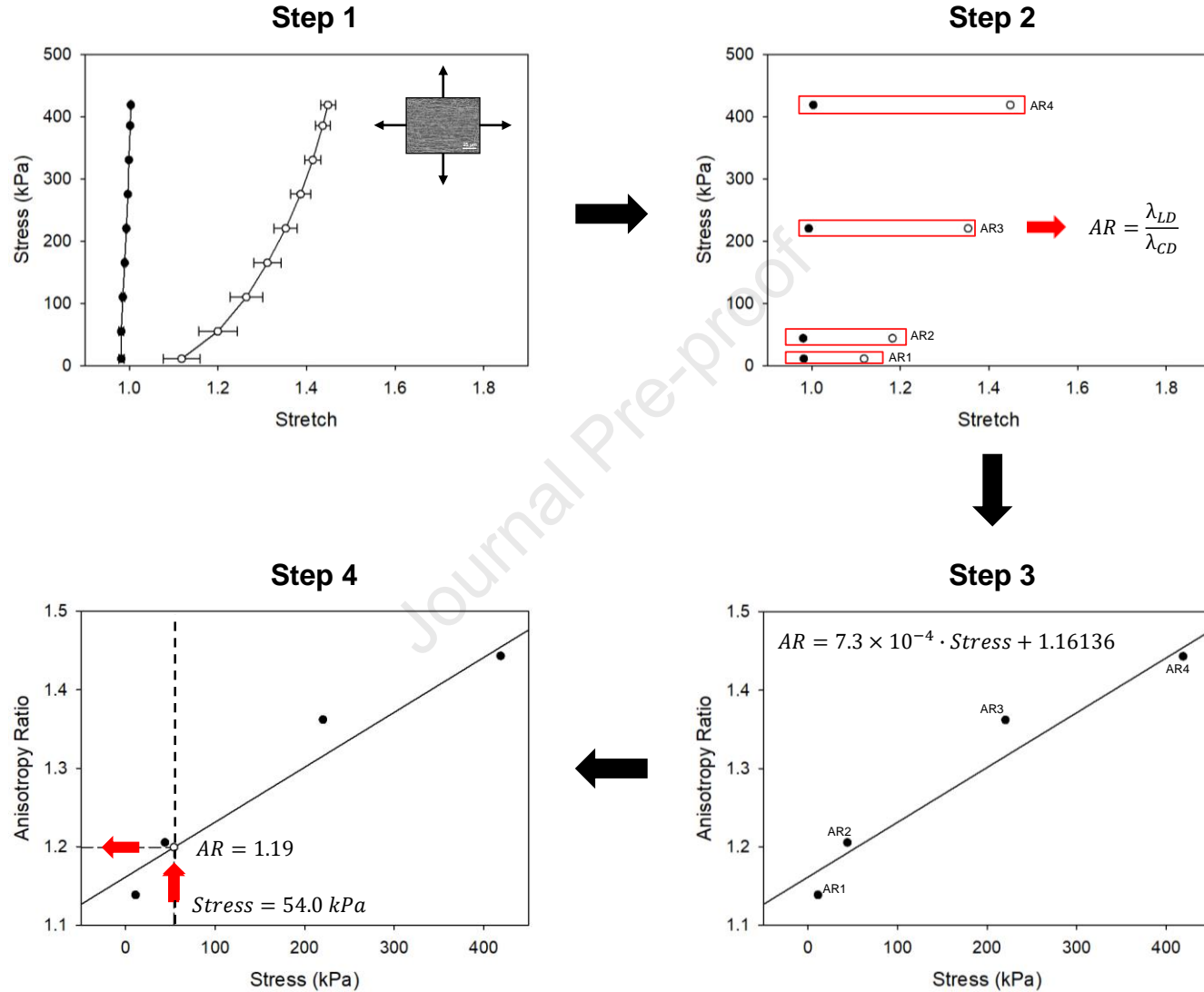


FIGURE 11



Declaration of interests

The authors declare that they have no known competing financial interests or personal relationships that could have appeared to influence the work reported in this paper.

The authors declare the following financial interests/personal relationships which may be considered as potential competing interests:

Journal Pre-proof